




Hydrophobic residues in the α -synuclein NAC domain drive seed-competent fibril formation and are targeted by peptide inhibitors

Viswanath Das^{1,2} , Sayed Mostafa Modarres Mousavi³, Narendran Annadurai¹, Sunčica Sukur¹, Faramarz Mehrnejad⁴, Sajad Moradi⁵, Lukáš Malina^{1,6}, Markéta Kolaříková⁶, Vaclav Ranc¹, Ivo Frydrych¹, Roman Kouřil⁷ , Saman Hosseinkhani⁸, Marián Hajdúch^{1,2} and Maryam Nikkhah³ 

1 Faculty of Medicine and Dentistry, Institute of Molecular and Translational Medicine, Palacký University and University Hospital Olomouc, Czech Republic

2 Institute of Molecular and Translational Medicine, Czech Advanced Technologies and Research Institute, Palacký University Olomouc, Czech Republic

3 Department of Nanobiotechnology, Faculty of Biological Sciences, Tarbiat Modares University, Tehran, Iran

4 Department of Nanobiotechnology and Biomimetics, School of Life Science Engineering, University of Tehran, Iran

5 Nano Drug Delivery Research Centre, Health Technology Institute, Kermanshah University of Medical Sciences, Iran

6 Department of Medical Biophysics, Faculty of Medicine and Dentistry, Palacký University Olomouc, Czech Republic

7 Department of Biophysics, Faculty of Science, Palacký University Olomouc, Czech Republic

8 Department of Biochemistry, Faculty of Biological Sciences, Tarbiat Modares University, Tehran, Iran

Keywords

alpha-synuclein; amyloid fibril; hydrophobic region; non-amyloid component; Parkinson's disease; peptide inhibitor; synuclein seeding

Correspondence

V. Das, Institute of Molecular and Translational Medicine, Faculty of Medicine and Dentistry, Palacký University and University Hospital Olomouc, Hněvotínská 1333/5, 779 00 Olomouc, Czech Republic
 Tel: +420 585 632 111
 E-mail: viswanath.das@upol.cz
 and

M. Nikkhah, Department of Nanobiotechnology, Faculty of Biological Sciences, Tarbiat Modares University, 14115-154 Tehran, Iran
 Tel: +98 21 82884734
 E-mail: m_nikkhah@modares.ac.ir

(Received 22 January 2025, revised 27 May 2025, accepted 1 August 2025)

doi:10.1111/febs.70222

Alpha-synuclein (α Syn) is a 14-kDa intrinsically disordered protein that aggregates into insoluble fibrils in synucleinopathies, including Lewy bodies, multiple system atrophy, and Parkinson's disease, contributing to neurotoxicity and disease progression. The ability of these fibrils to seed further aggregation of native protein is central to α Syn pathology. Here, we examined the broader non-amyloid component (NAC) domain, focusing on how residues flanking the hydrophobic 68–71 (GAVV) motif of α Syn (residues 8–11 in NAC35) modulate nucleation, stability, and pathological seeding. Using full-length NAC peptide and truncated variants, we show that the 68–71 (GAVV) stretch is critical for nucleation and aggregation into prion-like fibrils. Peptide inhibitors targeting this hydrophobic region block the formation of seed-competent fibrils. Molecular dynamics simulations showed that these inhibitors alter peptide–peptide interactions and contact key hydrophobic residues within the NAC domain. Further analysis indicates that residues beyond the 68–71 (GAVV) motif, such as 79–95, are critical for stabilizing fibrils and promoting seeding competency. Peptide B interactions with key hydrophobic motifs within the NAC domain were visualized *in silico*, offering mechanistic insights into how it disrupts aggregation.

Abbreviations

AFM, atomic force microscopy; ANS, 8-anilino-1-naphthalene-sulfonic acid; CFP, cyan fluorescent protein; MD, molecular dynamics; MSD, mean squared displacements; MST, microscale thermophoresis; NAC, non-amyloid component; PB, Peptide B; PD, D-amino acid peptide; PL, L-amino acid peptide; PS, scrambled peptide; RMSD, root mean squared deviation; SASA, solvent-accessible surface area; SPC/E, simple point charge extended; TEM, transmission electron microscopy; ThT, thioflavin T; UV-Vis, ultraviolet-visible; YFP, yellow fluorescent protein; α Syn, alpha-synuclein.

Introduction

Amyloid fibrils of alpha-synuclein (α Syn) are associated with dementia with Lewy bodies (DLB), multiple system atrophy, and Parkinson's disease [1–3]. These fibrils have been linked to neuronal death and neuroinflammation in cellular models [4,5]. α Syn aggregates show prion-like behavior, seeding further aggregation of native α Syn [6,7]. Beyond neurological diseases, α Syn is associated with cancers, suggesting a potential overlap in disease mechanisms [8,9]. Therefore, understanding the role of α Syn in one disease may help identify biomarkers and therapeutics for both diseases [10].

α Syn comprises an N-terminal region (1–60 aa) that adopts an α helix conformation when bound to membranes, a non-amyloid component (NAC) region (61–95 aa) critical for aggregation, and a C-terminal acidic tail (96–140 aa). The N-terminal region harbors several mutation sites (A53T, A30P, and E46K) linked to familial Parkinson's disease [11]. The non-NAC (P1 and P2) region is suggested to initiate α Syn aggregation by synergizing with the NAC and C-terminal regions [12]. However, the NAC domain forms the core folded region of α Syn aggregates, playing a critical role in the aggregation process [13–16]. Glu83 (E83) in the NAC acts as a negative regulator of amyloid formation, and mutations at this site, such as E83Q, accelerate aggregation and increase toxicity, as observed in DLB [2,17].

Previous studies by Giasson *et al.* and Bodles *et al.* have emphasized the role of broader regions, such as 68–76 and 71–82, within the NAC domain in promoting α Syn aggregation [18,19]. While these studies established the importance of hydrophobic stretch, they did not comprehensively address the specific contributions of flanking residues to aggregation dynamics and seeding competency. Our study extends these findings by systematically dissecting the broader NAC region and investigating inhibitors targeting critical residues, specifically, a previously validated peptide that mimics the 70–75 region of α Syn [20], which overlaps with the nucleation-critical segment identified in our study. Understanding the role of specific residues is crucial, as even minor changes in this highly conserved sequence can profoundly influence aggregation dynamics and toxicity [17,18]. Using full-length hydrophobic NAC peptide and its truncated variants, we demonstrated the critical role of 68–71 (GAVV) residues in both the aggregation propensity and the seeding competency of the NAC region, findings not previously reported. Additionally, residues beyond this region, including residues 79–95, were shown to promote stable fibril formation and seeding activity. These

findings highlight the complexity of α Syn aggregation and underscore the importance of considering the entire NAC region, not just the core hydrophobic stretch, in understanding α Syn aggregation.

Results

Truncation of residues 61–62 and 79–95 enhances NAC aggregation

Six distinct NAC peptides were generated by truncating specific regions of the NAC domain. NAC35 included the entire NAC domain, while NAC8 represented the shortest peptide, consisting of only eight residues (Fig. 1A). NAC11 (corresponding to α Syn 68–78), corresponding to the minimal toxic core described by Rodriguez *et al.* [16], was included to evaluate the role of this core in aggregation dynamics and fibril formation. Hydrophathy analysis of these peptides was performed as described previously [21], revealing varying hydrophobic and hydrophilic characteristics across the sequences. NAC35 exhibited strong hydrophobicity at positions 8–12, whereas shorter peptides like NAC8 were predominantly hydrophilic (Fig. 1A).

The aggregation kinetics showed that NAC35 (corresponding to α Syn 61–95), NAC16 (corresponding to α Syn 63–78), and NAC11 (corresponding to α Syn 68–78) readily underwent aggregation, which correlates with their prominent hydrophobic peaks (1.84, 1.84, and 2.30, respectively; Fig. 1B). In contrast, NAC17 (corresponding to α Syn 79–95), NAC12 (corresponding to α Syn 71–82), and NAC8 (corresponding to α Syn 72–79), with lower hydrophobicity scores, did not aggregate. The presence of β -sheet-rich aggregates was also confirmed by fluorescence microscopy (Fig. S1). Notably, ThT curves of both NAC16 and NAC11 rapidly increased to a peak with a short plateau, followed by a decrease toward the starting point (Fig. 1B).

Next, we calculated the aggregation lag time using ThT readings between 0 and 10 h since this window corresponded to when NAC35, NAC16, and NAC11 aggregation curves reached their maximum peak. Truncated NAC16 and NAC11 peptides displayed a shorter lag time of aggregation than NAC35 (Fig. 1C).

Atomic force microscopy (AFM) and transmission electron microscopy (TEM) imaging revealed that NAC35 and NAC16 formed elongated fibrils with clumped tangles, whereas NAC11 aggregated into dense, sticky bundles lacking elongated tangles (Fig. 1D). In contrast, no fibrillar or aggregated structures were formed by NAC17, NAC12, and NAC8

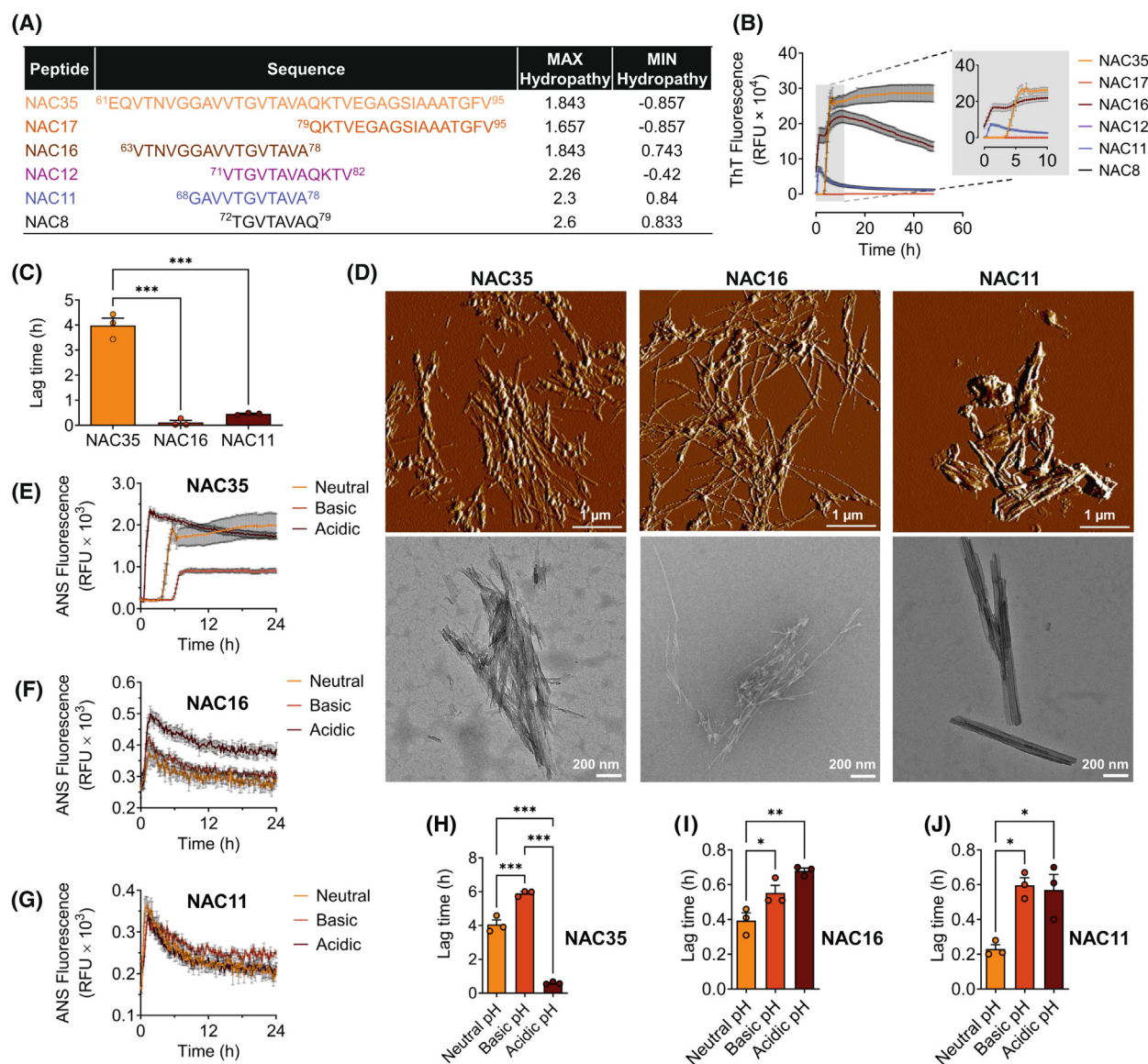


Fig. 1. Truncation and pH modulate aggregation kinetics of NAC35, NAC16, and NAC11. (A) Amino acid sequences of the six NAC peptides used in the study. (B) Aggregation kinetics of NAC peptides over time, with the inset (gray box) showing the first 10 h of aggregation kinetics. (C) Lag time of NAC35, NAC16, and NAC11 aggregation, extracted from the first 10 h of data. (D) AFM (atomic force microscopy) and TEM (transmission electron microscopy) images of NAC aggregates after 48 h of aggregation. Scale bars: 1 μ m (AFM) and 200 nm (TEM). (E–G) Aggregation kinetics of NAC peptides in neutral (pH 7.2), basic (pH 8.0), and acidic (pH 4.5) buffers. (H–J) Lag time of NAC35, NAC16, and NAC11 aggregation under neutral, basic, and acidic conditions. Mean \pm SEM ($n = 3$ independent experiments), * $P \leq 0.05$, ** $P \leq 0.01$, *** $P \leq 0.001$ (One-way ANOVA). F values and degrees of freedom are provided in the [Supplementary Material](#). See Data Availability for access to source data (B) and (D–F).

after 48 h (Fig. S1), consistent with their inability to aggregate.

pH sensitivity of NAC aggregation

An 8-anilidonaphthalene-1-sulfonic acid (ANS) assay, which detects exposed hydrophobic regions [22], was

performed to investigate how pH variations affect the aggregation behavior of NAC peptides. Altering pH did not induce NAC17, NAC12, and NAC8 aggregation. However, pH variations significantly influenced NAC35, NAC16, and NAC11 aggregation kinetics (Fig. 1E–G). For NAC35, acidic pH shortened the lag time while basic pH increased it. In contrast, NAC16

and NAC11 exhibited longer lag times under acidic and basic conditions than neutral pH (Fig. 1H–J).

Solubility does not explain the lack of aggregation in NAC17, NAC12, and NAC8

Hydropathy profiles indicated that NAC17, NAC12, and NAC8 were predominantly hydrophilic (Fig. 1A). UV–Vis spectrophotometry confirmed their solubility by showing indistinguishable spectra for soluble and insoluble fractions after incubation (Fig. 2). In contrast, aggregating peptides (NAC35, NAC16, NAC11) exhibited a clear increase in absorbance in the insoluble fraction, consistent with aggregate formation (Fig. 2; Fig. S2).

Structural changes of NAC35, NAC16, and NAC11 upon aggregation were further analyzed by Raman spectroscopy. The spectra of NAC35, NAC16, and NAC11 showed structural changes, marked by the increase in amide band intensities and new spectral signals (Fig. S3).

NAC35 but not NAC16 and NAC11 preformed fibrils seed α Syn aggregation

Since Raman spectra of NAC35, NAC16, and NAC11 revealed amide band shifts, suggestive of β -sheet

changes [23], we examined whether their aggregates could act as seeds. Kinetics data showed that NAC35 fibrils, but not NAC16 and NAC11, significantly shortened the lag time of α Syn aggregation (Fig. 3A). Baseline correction was performed using stable ThT fluorescence values from preformed fibrils, as shown in Fig. S4. Although NAC16 and NAC11 form fibrils (Fig. 1D), they fail to seed α Syn aggregation, unlike NAC35 (Fig. 3A). α Syn seeded with preformed α Syn fibrils showed no detectable lag phase, indicating immediate aggregation, whereas unseeded α Syn aggregated with a longer lag time. Dot blot analysis confirmed the ThT results, revealing increased insoluble fractions in α Syn seeded with NAC35 fibrils (Fig. 3B). Quantifying dimer-to-monomer band ratios showed that preformed NAC35 fibrils, like α Syn fibrils, significantly increased α Syn dimerization (Fig. 3C,D). The full uncropped images of the dot blot and gel are shown in Fig. S5.

Peptide inhibitors reduce dimerization and aggregation of α Syn

Building on our findings that the presence of residues 8–11 in NAC peptides, corresponding to α Syn 68–71, is necessary for efficient nucleation and aggregation, we investigated whether disrupting this hydrophobic

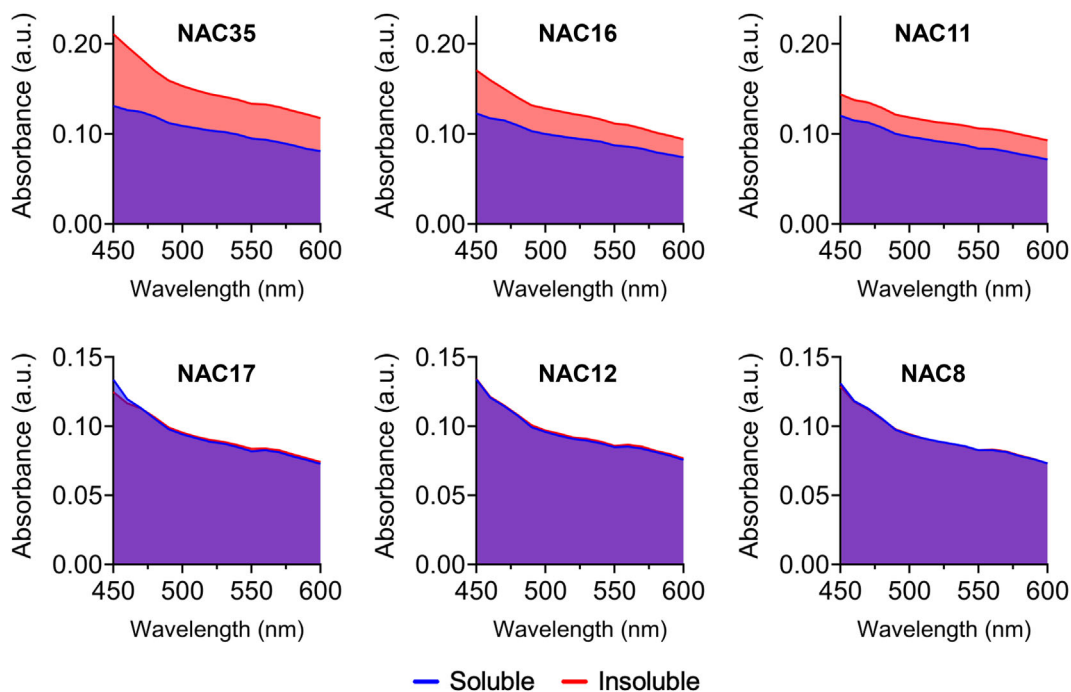


Fig. 2. Solubility does not explain the lack of aggregation of NAC17, NAC12, and NAC8. UV–Vis absorption spectra of soluble and insoluble fractions of NAC peptides after 48 h of aggregation. Data represent the means of 3 replicates. See Data Availability for access to source data.

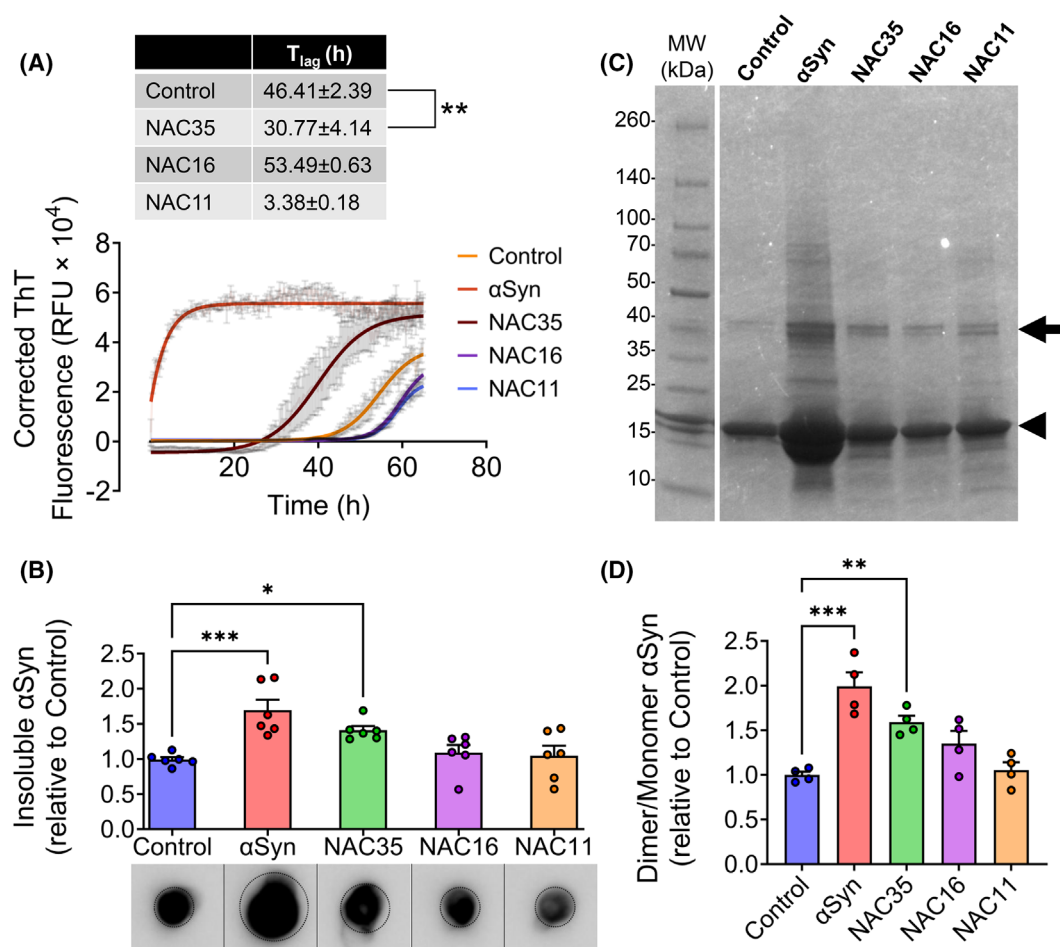


Fig. 3. Preformed NAC35 fibrils seed monomeric α Syn aggregation. (A) Aggregation kinetics of monomeric α Syn seeded without (Control) or with preformed fibrils of α Syn, NAC35, NAC16, and NAC11 (4 : 1 monomer: seed ratio). Preformed α Syn fibrils were used as positive controls. Baseline correction was applied using stable ThT (thioflavin T) fluorescence values from preformed fibrils (Fig. S4) to ensure accurate quantification of seeded aggregation. The lag time for each condition is indicated. For α Syn seeded with preformed α Syn fibrils, the lag time was not calculated due to the absence of a detectable lag phase. (B) Quantification and dot blot analysis of insoluble fractions of α Syn aggregated for 72 h in the absence (control) or presence of preformed fibrils of α Syn, NAC35, NAC16, and NAC11. Dotted circles indicate the regions used for quantification. Vertical lines denote where the blot layout was adjusted to align sample lanes. The original, unmodified dot blot image is provided in Fig. S5. (C) Coomassie-stained gel of insoluble fractions showing monomer (arrowhead) and dimer (arrow) bands. The full-length gel image is shown in Fig. S5. (D) Quantification of the dimer-to-monomer band ratio showing increased α Syn dimerization in the presence of preformed α Syn and NAC35 fibrils. Mean \pm SEM [$n = 3$ independent experiments for dot blot (B) and $n = 2$ for gel (D)], Control vs. Fibril-seeded, * $P \leq 0.05$, ** $P \leq 0.01$, *** $P \leq 0.001$ (One-way ANOVA). F values and degrees of freedom are provided in the [Supplementary Material](#). See Data Availability for access to source data for (A).

region could inhibit full-length α Syn aggregation. Truncating these residues abolished aggregation, and peptides containing them (e.g., NAC16, NAC11) aggregated rapidly (Fig. 1). To test whether targeting this site could suppress aggregation, we selected a previously validated inhibitor peptide based on the KISVRV sequence [20]. This segment mimics the 70–75 region of α Syn, a hydrophobic subregion overlapping with the 68–71 nucleation motif and implicated in fibril initiation [20]. This core sequence has

been shown to inhibit α Syn fibril formation and dissolve preformed oligomers and was designed to engage the NAC domain through sequence and physicochemical complementarity [20].

In this study, we used an extended form of the previously validated KISVRV inhibitory sequence, adding a poly-arginine tail (RRRRRR) to generate the full sequence KISVRVRRRRR, which was common to all peptide variants tested. To enable future cellular applications, we synthesized three modified variants:

peptide D (PD, composed of D-amino acids), peptide L (PL, composed of L-amino acids), and peptide B (PB, with an acetylated C terminus) (Fig. 4A). Potential effects related to stereochemistry, terminal modification, or the poly-arginine tail extension were not evaluated in the present study. All inhibitor peptides contained the same KISVRV core sequence, previously shown to block α Syn fibrillation and disrupt pre-formed oligomers [20]. A scrambled control peptide (VSRKIVRRRRR), containing the same amino acid composition in a randomized sequence, was used to assess sequence specificity. This design follows the approach described previously [20], in which scrambled peptides (PS) preserve composition while eliminating motif-specific interactions.

The affinity of PD, PL, PB, and a scrambled control peptide (PS) for α Syn was determined by microscale thermophoresis (MST). MST results showed a higher affinity of all inhibitor peptides for full-length α Syn than the PS peptide (Fig. 4B; Fig. S6). While MST with full-length α Syn successfully demonstrated the binding affinity of the inhibitors, attempts to use MST with truncated NAC peptides were not feasible due to technical challenges. Specifically, the small size and reduced structural stability of the NAC peptides hindered efficient fluorescent labeling (data not shown), which is essential for MST analysis and compromised the thermophoretic shifts required for reliable detection.

The effect of inhibitors on α Syn aggregation was evaluated by incubating α Syn with PD, PL, and PB at a 1 : 2 molar ratio and then monitoring aggregation by ThT assay. The kinetics data revealed that PD, PL, and PB are highly effective in inhibiting α Syn aggregation (Fig. 4C). To quantify the extent of inhibition, the final ThT reading for each treatment was normalized to that of the control group, providing a relative comparison of amyloid fibril formation. This analysis revealed that all inhibitors significantly reduced α Syn fibrils compared to the control (Fig. 4D). TEM analysis corroborated ThT results, showing reduced fibril density in the presence of inhibitors (Fig. 4E). The increase in α Syn aggregation in the presence of PS is likely due to its non-specific binding (Fig. 4D), given that fibril morphology was unaffected (Fig. S7). PD, PL, PB, and PS peptides showed no signs of self-aggregation (Fig. S8). Dot blot analysis and Coomassie staining revealed that inhibitors reduced the formation of insoluble fibrils and significantly decreased the dimer-to-monomer ratio of α Syn (Fig. 4F–I). The full uncropped images of the dot blot and gel are shown in Figs S9 and S10.

α Syn fibrils formed in the presence of inhibitors have reduced seeding competency

Given that the inhibitors reduced α Syn dimerization, we next investigated the seeding competency of α Syn fibrils formed with inhibitors. To this end, we used HEK293T biosensor cells stably expressing α Syn (A53T) CFP/YFP-tagged fusion proteins and quantified intracellular seeding using confocal microscopy and FRET flow cytometry, following the method described in the original study [24].

α Syn was incubated with PD, PL, and PB at a molar ratio of 1 : 2 for 72 h, after which the samples were collected and either used as a total fraction or separated into insoluble fractions by pelleting assay. To ensure consistency across all conditions, we measured the concentration of α Syn fibrils in each sample and used an equal concentration (1 μ M) of total or insoluble fractions for cell transduction. This approach ensured that any observed differences in intracellular seeding are due to the structural and functional properties of the fibrils formed in the presence or absence of inhibitors rather than variations in the amount of α Syn fibrils applied.

Fluorescent CFP/YFP inclusions were not observed in the absence of exogenous fibrils (Fig. 5A) or when cells were transduced with fibrils without the TurboFect transfection reagent (Fig. S11), consistent with previous reports that liposome-mediated transduction facilitates efficient seeding in these biosensor cells [24]; though passive uptake of sonicated fibrils has also been shown to induce seeding [25]. Cells transduced with fibrils formed in the presence of inhibitor peptides exhibited significantly fewer CFP/YFP inclusions than those transduced with control total or insoluble α Syn fibrils (Fig. 5B–D). PB was the most effective in reducing the seed competency of α Syn fibrils compared to the other inhibitors (Fig. 5C,D). The inhibitor peptides alone did not induce seeding, as cells transduced with only the inhibitors showed no CFP/YFP inclusions (Fig. S11). FRET cytometry data further corroborated our CFP/YFP inclusion count results (Fig. 5E), confirming the reliability of inclusion counting as demonstrated in this study [26].

Sequence-specific modulation of NAC peptide aggregation by inhibitor peptides

To further investigate the region-specific effects of inhibitor peptides on aggregation, we studied their interactions with NAC peptides. By focusing on NAC35, NAC16, and NAC11, we aimed to identify aggregation-prone stretches within the NAC domain.

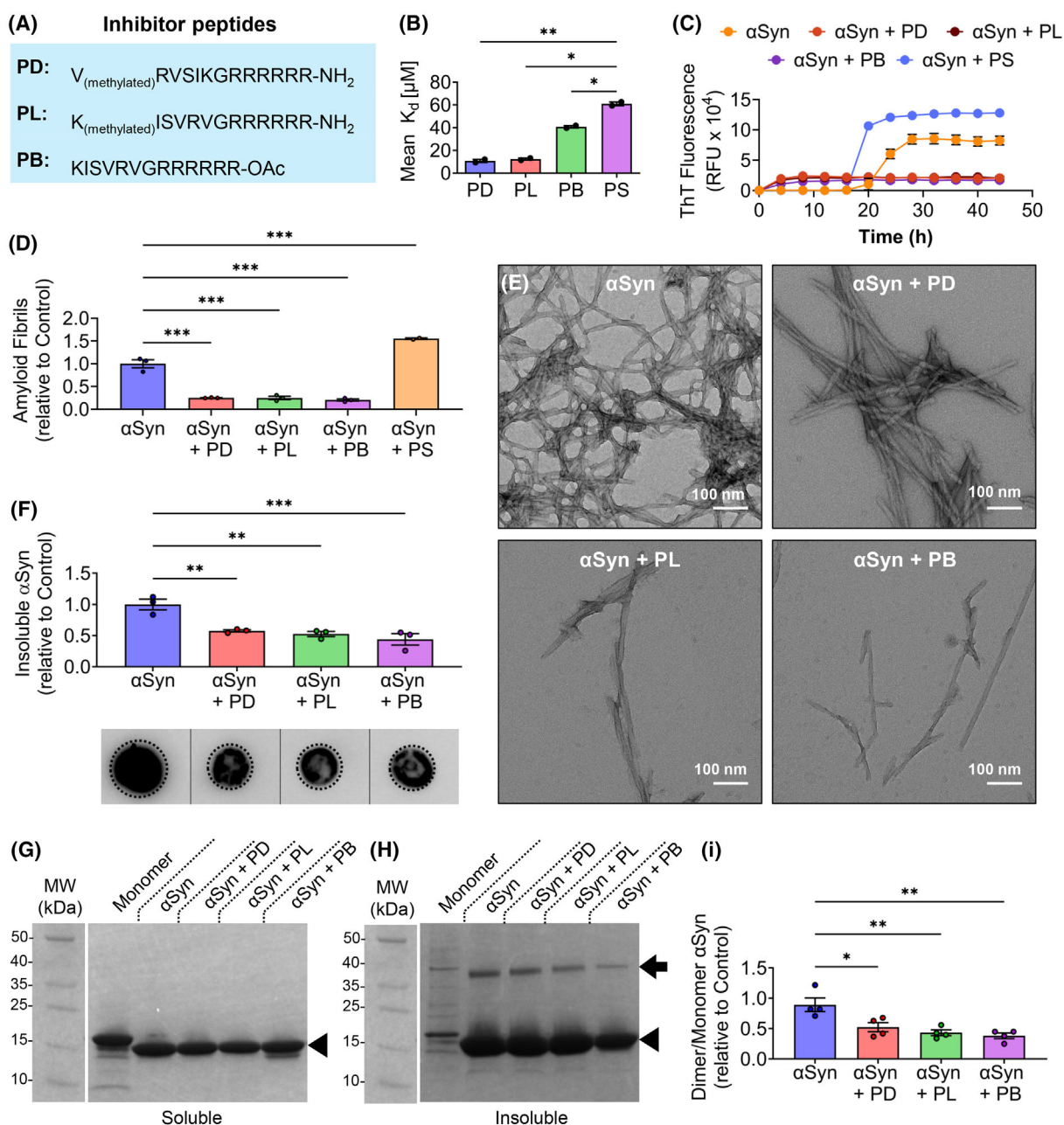


Fig. 4. Inhibitor peptides targeting the hydrophobic region of α Syn reduce aggregation and modify fibril characteristics. (A) Sequences of PD (peptide D), PL (peptide L), and PB (peptide B) inhibitors. (B) Binding affinity (K_d) of inhibitor peptides binding to α Syn. (C) Aggregation kinetics of α Syn in the absence or presence of PD, PL, PB, and PS (scrambled peptide) peptides. (D) Final ThT (thioflavin T) fluorescence readings quantifying amyloid fibrils formed at the end of the aggregation assay. (E) TEM (transmission electron microscopy) images of α Syn fibrils formed with or without PD, PL, or PB inhibitors. Scale bar: 100 nm. (F) Quantification and dot blot analysis of insoluble fractions of α Syn aggregated in the absence or presence of PD, PL, and PB. Dotted circles indicate the regions used for quantification. Vertical lines denote where the blot layout was adjusted to align sample lanes. The original, unmodified dot blot image is provided in Fig. S9. (G, H) Coomassie-stained gel showing monomer (arrowheads) and dimer (arrow) bands in soluble (G) and insoluble (H) fractions for the indicated samples. Images of uncropped gels are shown in Fig. S10. (I) Dimer-to-monomer band ratio quantification in the insoluble fraction. Mean \pm SEM [$n = 3$ independent replicates except for α Syn + PS in panel (C) where $n = 2$], $*P \leq 0.05$, $**P \leq 0.01$, $***P \leq 0.001$ (One-way ANOVA). F values and degrees of freedom are provided in the Supplementary Material. See Data Availability for access to source data for (C).

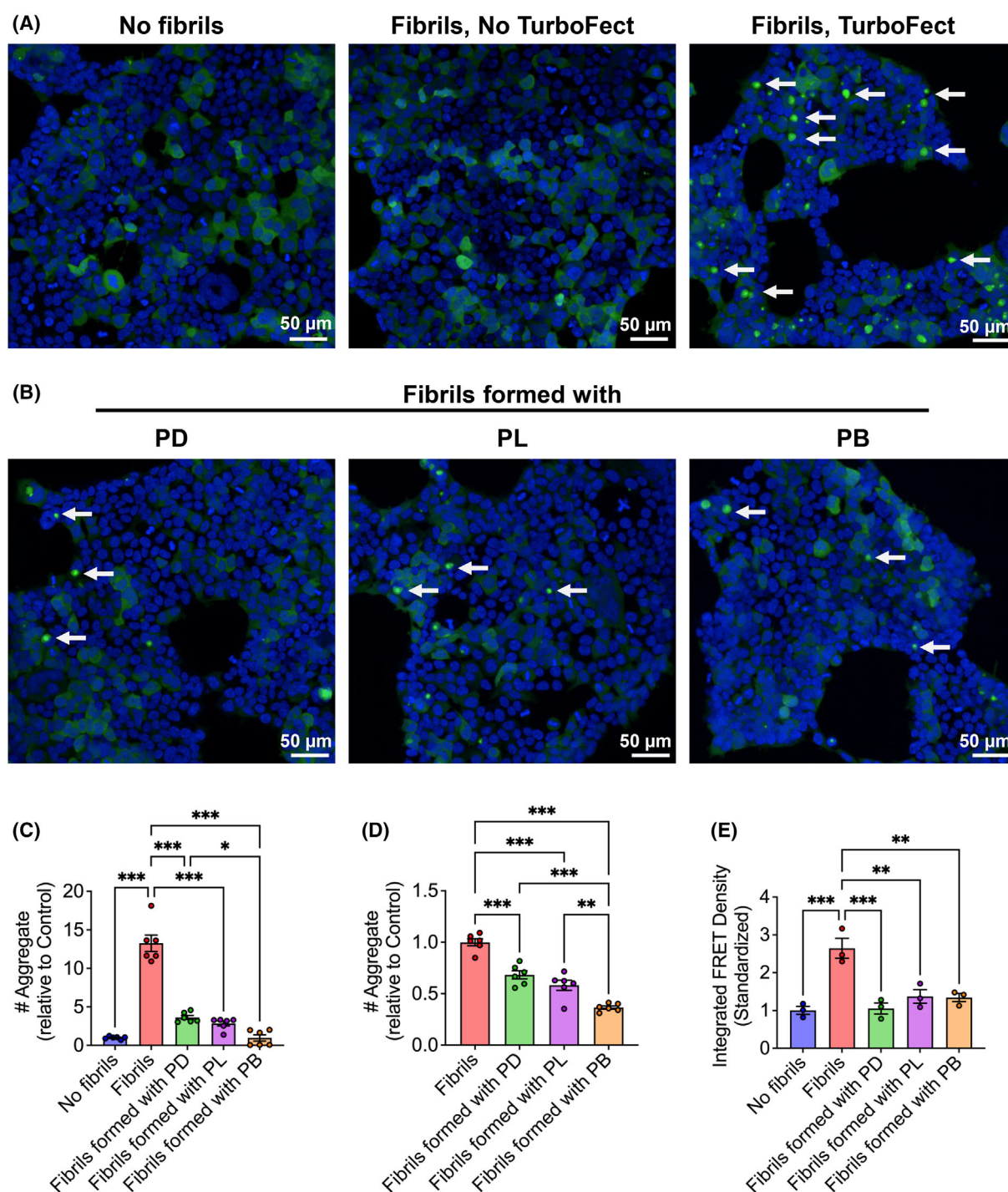


Fig. 5. Inhibitor peptides prevent the formation of seed-competent α Syn fibrils. (A, B) Confocal images of biosensor cells transduced with α Syn fibrils from the total fraction. CFP (cyan fluorescent protein)/YFP (yellow fluorescent protein) inclusions (white arrows) are absent without fibril transduction but appear with fibrils in the presence of TurboFect. Cells treated with PD (peptide D), PL (peptide L), or PB (peptide B) fibrils show reduced inclusions. Hoechst-33342 staining is blue. Scale bar: 50 μ m. (C, D) Number of CFP/YFP inclusions in cells transduced with α Syn fibrils from the total fraction (C) or insoluble fraction (D). (E) Standardized integrated FRET (fluorescence resonance energy transfer) density of cells transduced with α Syn fibrils formed with or without inhibitors from the total fraction. Scatter plots showing the gating of cells are shown in Fig. S11. Mean \pm SEM ($n = 3$ independent experiments), $*P \leq 0.05$, $**P \leq 0.01$, $***P \leq 0.001$ (one-way ANOVA). F values and degrees of freedom are provided in the [Supplementary Material](#). See Data Availability for access to source data for (C–E).

NAC16 (63–78) and NAC11 (68–78) aggregated efficiently, whereas peptides lacking these residues did not aggregate (Fig. 1). NAC peptides were incubated with inhibitor peptides at a 1 : 2 molar ratio, and aggregation was monitored by ThT assay in the neutral buffer. Control experiments demonstrated that inhibitor peptides showed no signs of self-aggregation (Fig. S7). The results revealed distinct inhibitory effects on NAC peptide aggregation: inhibitors shortened the lag time of NAC35 aggregation (Fig. 6A,D), while significantly increasing the lag time of NAC16 and NAC11 aggregation (Fig. 6B,C,E,F). Despite the reduced lag time of NAC35 aggregation, the total amount of amyloid fibrils formed was markedly lower in the presence of inhibitors (Fig. 6G).

This observation was corroborated by scanning electron microscopy (SEM) analysis (Fig. 7). In the absence of inhibitors, NAC35 formed dense networks of long, bundled fibrils. Inhibitor-treated NAC35, particularly with PB, contained visibly shorter fibrils that were less bundled and appeared fragmented. NAC16 formed continuous fibrils under control conditions, while PD, PL, and PB treatments resulted in shorter, discontinuous fibrillar structures. NAC11 formed large, clustered fibrils that extended beyond the field

view at the magnification used for NAC35 and NAC16. To allow comparison, NAC11 samples were imaged at a lower magnification (Fig. S12). In the presence of inhibitors, NAC11 showed reduced fibril continuity and more dispersed fragments at both magnifications (Fig. 7; Fig. S12). No distinct morphologies or additional structures were observed that would indicate heterogeneous co-aggregation between inhibitors and NAC peptides. The inhibitors alone did not form fibrillar or amorphous aggregates (Fig. S13).

PB inhibitor disrupts NAC aggregation dynamics through structural instability

Molecular dynamics (MD) simulations were performed to assess how PB interacts with NAC peptides and alters their structural behavior. In the absence of PB, NAC peptides exhibited extensive intermolecular hydrogen bonding (Fig. 8). However, in systems containing PB, the number of NAC–NAC hydrogen bonds decreased, while NAC–PB hydrogen bonding increased.

The root mean square deviation (RMSD) values of the C α atoms showed consistently higher values in NAC + PB systems compared to NAC-only systems

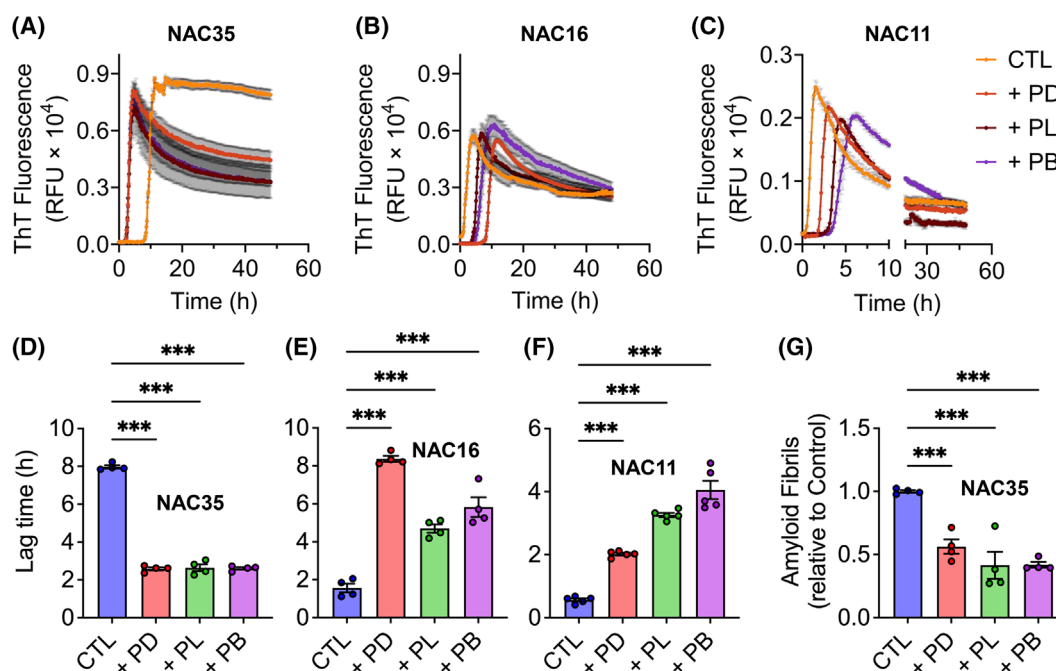


Fig. 6. Inhibitor peptides modulate NAC aggregation kinetics and lag times. (A–C) Aggregation kinetics of NAC35, NAC16, and NAC11 without (CTL) or with PD (peptide D), PL (peptide L), and PB (peptide B) inhibitors. (D–F) Lag time of aggregation in the absence (CTL) or presence of inhibitor peptides. (G) Final ThT fluorescence readings quantifying amyloid fibril formation at the end of the aggregation assay. Mean \pm SEM ($n = 4$ independent experiments), *** $P \leq 0.001$ (One-way ANOVA). *F* values and degrees of freedom are provided in the [Supplementary Material](#). See Data Availability for access to source data for (A–C).

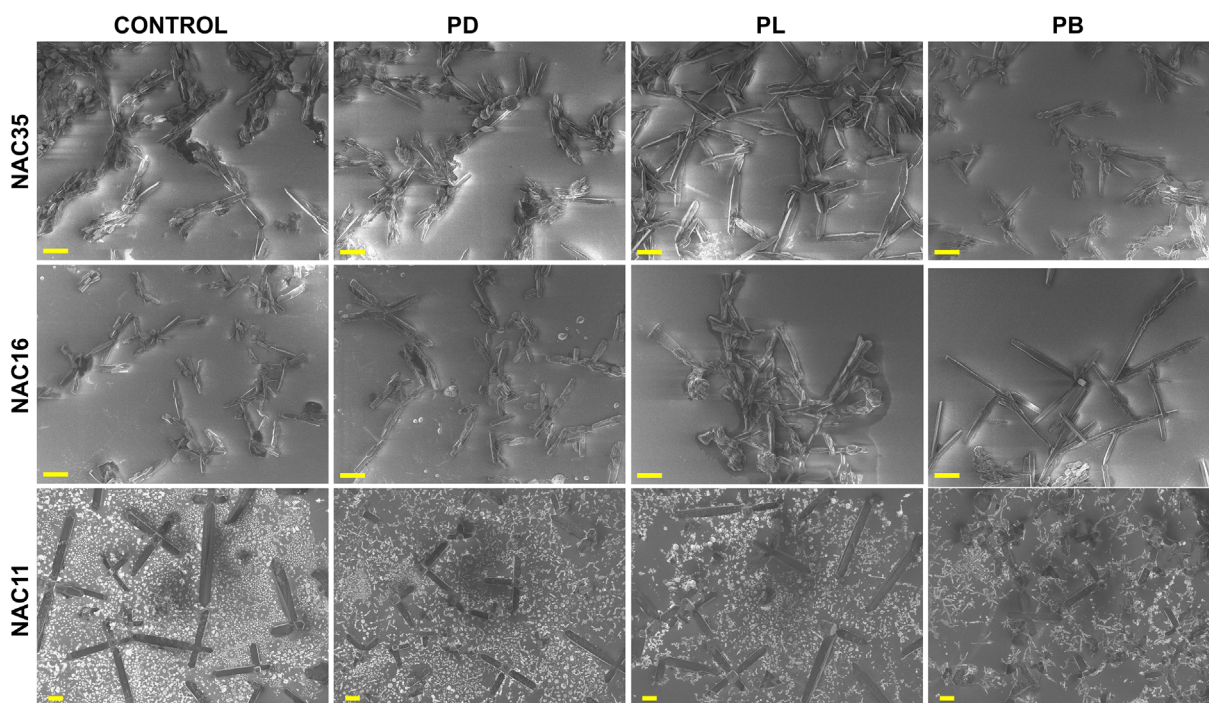


Fig. 7. Fibril fragmentation is visible in NAC peptide samples treated with inhibitors. SEM (scanning electron microscopy) images of NAC35, NAC16, and NAC11 fibrils formed in the absence (control) and presence of PD (peptide D), PL (peptide L), and PB (peptide B) inhibitors. Scale bar: 10 μ m (NAC35 and NAC16) and 50 μ m (NAC11). Higher-magnification NAC11 images are provided in Fig. S12.

(Fig. 9A). This pattern was observed across all three NAC peptides, with NAC11 + PB exhibiting the highest RMSD. Solvent-accessible surface area (SASA) values were also higher in NAC + PB systems than in NAC-only systems (Fig. 9B).

To assess residue-specific interactions between NAC peptides and the PB inhibitor, we quantified the number of contacts formed by each NAC residue with PB throughout the simulation (Fig. 10). The contact heatmaps revealed that NAC11 formed the most extensive and persistent interactions with PB, particularly across residues Ala69 to Ala78 (Fig. 10A). In NAC16, PB primarily contacted two regions: Gly67 to Val70 and Val77 to Ala78 (Fig. 10B). For NAC35, PB interactions were more dispersed, with notable contact frequencies observed in two regions: Val66 to Ala69 and Glu83 to Ala85 (Fig. 10C).

Representative molecular frames extracted at $T = 0$ and $T = 1000$ ns show that PB remained structurally stable and maintained consistent interactions with NAC peptides over the stimulation period (Fig. 11). In the absence of PB, NAC peptides appeared visually clustered into compact groupings by the end of the 1 μ s simulation. In contrast, in the presence of PB, the peptides remained spatially separated and extended, with no evident clustering.

Discussion

Prion-like propagation of α Syn aggregation is a critical pathological process in synucleinopathies, with the NAC domain (61–95) forming the core of aggregates [13–16]. This study addresses gaps in understanding how residues in and around the NAC contribute to aggregation, fibril stability, and prion-like behavior. By systematically testing truncated NAC peptides, we reveal distinct contributions of residues within and flanking the 71–82 core sequence to aggregation dynamics, nucleation, fibril stability, and seeding competency.

Previous studies have identified key sequences within the NAC domain, including the 71–82 region, the 68–76 stretch, and the toxic NACore fragment [16,18,19]. While these studies established the role of the 68–82 region in aggregation, they did not explore how residues flanking the core region contribute to nucleation efficiency, fibril stability, and prion-like behavior. In contrast, our study systematically dissected the NAC region, pinpointing the unique contributions of residues 68–71 and their interactions with adjacent sequences.

We provide evidence that truncating 68–71 (GAVV) abolishes aggregation, as NAC12 and NAC8, which

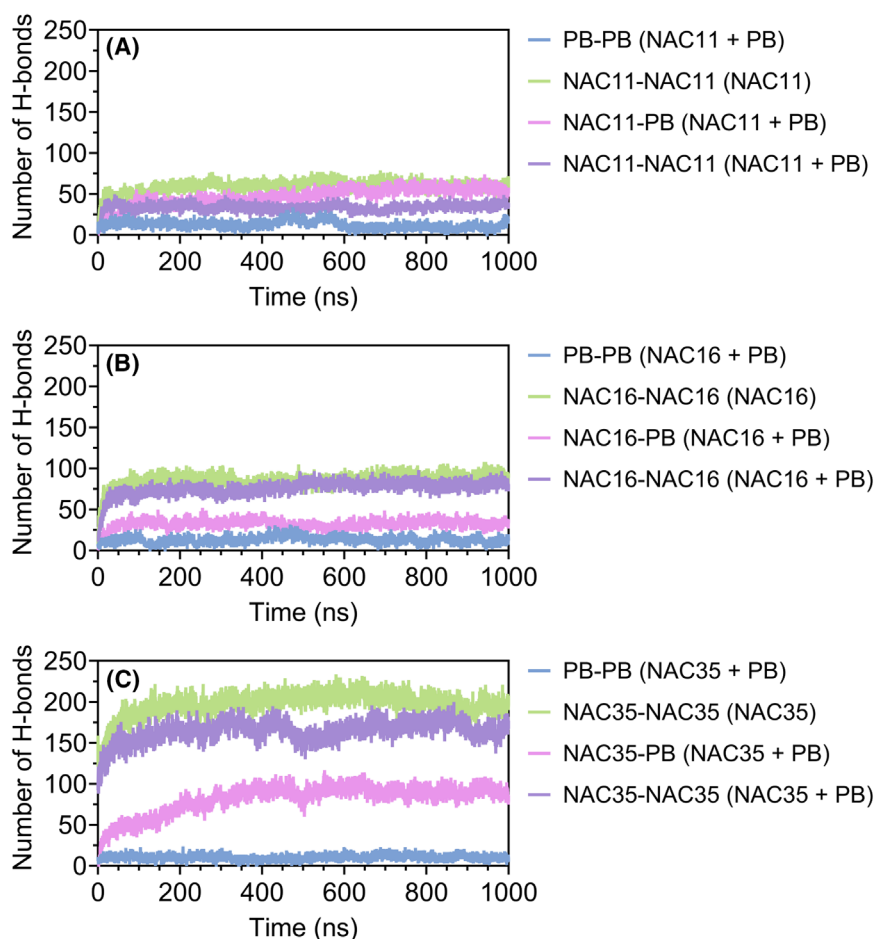


Fig. 8. Hydrogen bond distribution in NAC and NAC + PB systems. The number of hydrogen bonds is shown for each simulated system: NAC-only (NAC) and NAC in the presence of PB (peptide B) inhibitor (NAC + PB). NAC–NAC refers to hydrogen bonds between NAC peptides, NAC–PB to hydrogen bonds between NAC and PB, and PB–PB to hydrogen bonds between PB peptides. Single-trajectory simulation; representative results are shown. See Data Availability for access to source data.

lack these residues, do not aggregate, highlighting their essential role in nucleation. While the 71–88 region promotes aggregation in NAC35 (61–95), it is insufficient alone, as demonstrated by the lack of aggregation in NAC12 (71–82). In contrast, peptides such as NAC16 (63–78) and NAC11 (68–78), which include flanking residues, aggregate efficiently, underscoring the critical contributions of regions outside the core stretch. Our results clarify that aggregation involves a broader interplay of residues, demonstrating that flanking residues stabilize fibril structures and enhance aggregation kinetics.

This interpretation is supported by Raman spectroscopy, which revealed band shifts and increased intensities in NAC35, NAC16, and NAC11 - changes characteristic of β -sheet formation and consistent with those observed in α Syn fibrils [23]. In contrast, peptides

such as NAC17, NAC12, and NAC8 failed to aggregate under the same conditions. This lack of aggregation appears to result from insufficient hydrophobic interactions rather than poor solubility, as these peptides remained fully soluble throughout the assays.

While previous reports and our hydropathy analysis identified multiple hydrophobic segments across the NAC region, our focus was specifically on α Syn residues 68–71 (corresponding to NAC residues 8–11). Although residue 72 is threonine and polar, we observed that truncating just beyond Val71 abolishes aggregation entirely, highlighting 68–71 (GAVV) as likely the minimal nucleation motif. Other hydrophobic stretches, such as residues 88–91, were not explored in this study because they did not appear within the aggregation-prone motifs identified by prior structural studies and our experimental truncations. Moreover,

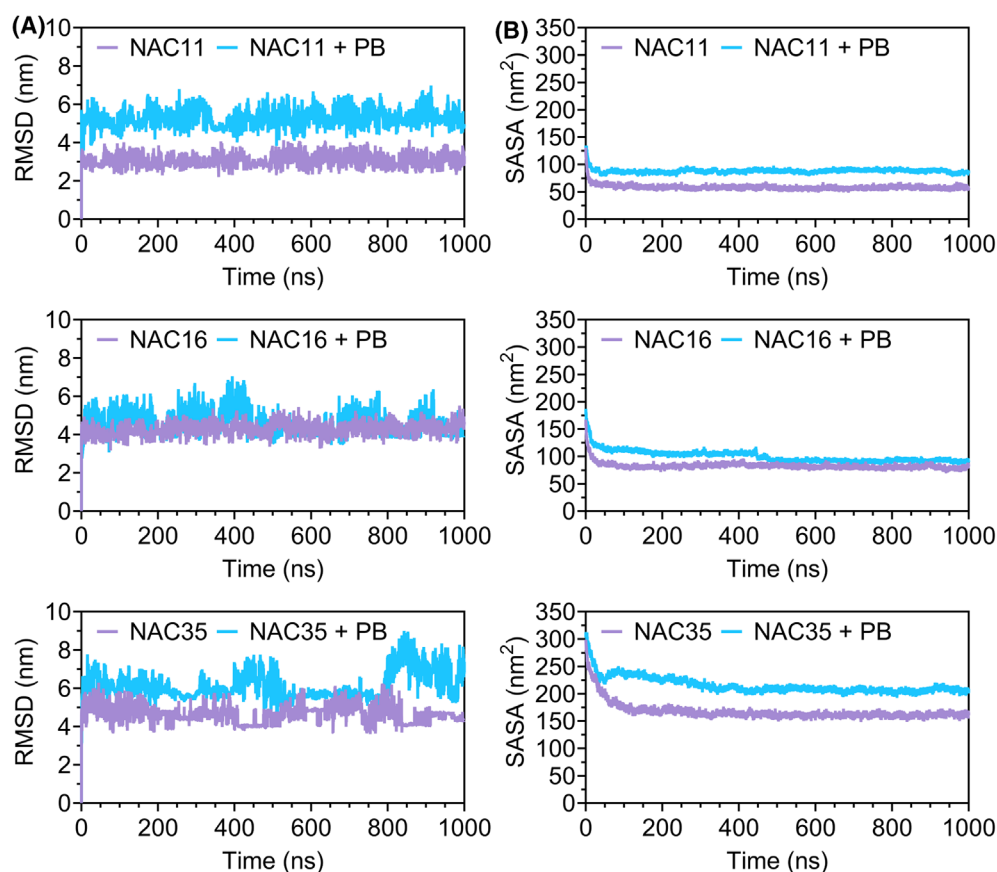


Fig. 9. RMSD and SASA profiles of NAC peptides in the presence and absence of PB. (A) Root mean square deviation (RMSD) over the 1000 ns molecular dynamics simulation for NAC-only and NAC + PB (peptide B) systems. (B) Solvent-accessible surface area (SASA) measurements for NAC peptides in the same systems. Single-trajectory simulation; representative results shown. See Data Availability for access to source data.

residues 68–71 displayed distinct responsiveness to pH variation in our aggregation assays, making them a particularly suitable and experimentally tractable focal point.

We show that residues outside the core hydrophobic stretch (68–78) influence aggregation behavior under different pH conditions. This includes hydrophobic residues such as 8–11 in NAC35 (corresponding to α Syn 68–71), 6–8 in NAC16 (corresponding to α Syn 68–70), and 4 and 7 in NAC11 (corresponding to α Syn 71 and 74), which may contribute to the observed pH-dependent changes in aggregation lag time. Waxman *et al.* identified hydrophobic stretches, including residues 71–82 and 74–79, in α Syn amyloid formation [17]. Our findings extend this by demonstrating that residues beyond the core 71–82 stretch, such as those in NAC35, contribute significantly to aggregation stability and dynamics, particularly under acidic conditions. The pH-dependent effects of NAC35 aggregation likely result from the protonation or

deprotonation of ionizable residues, modulating hydrophobic and electrostatic interactions critical for aggregation. Our observation of NAC35 aggregation in an acidic buffer aligns with the mechanism described by Hoyer *et al.* [22], where lower pH conditions reduce electrostatic repulsion among acidic residues such as Asp and Glu due to increased protonation, thereby promoting aggregation. We also observed that aggregating NAC35 in a basic buffer (pH 8.0) increased the aggregation lag time. Although not directly examined previously, we speculate that this effect may be explained by destabilized hydrophobic interactions involving residues such as Val66, Val70, and Val74 [18,19], and by enhanced electrostatic repulsion, presumably arising from the deprotonation of Glu83 under basic conditions [17].

Aggregation kinetics, as reflected in lag time (nucleation efficiency) and the endpoint fibril amount, indicating fibril stability, further demonstrate the functional roles of NAC peptides. While NAC16 and

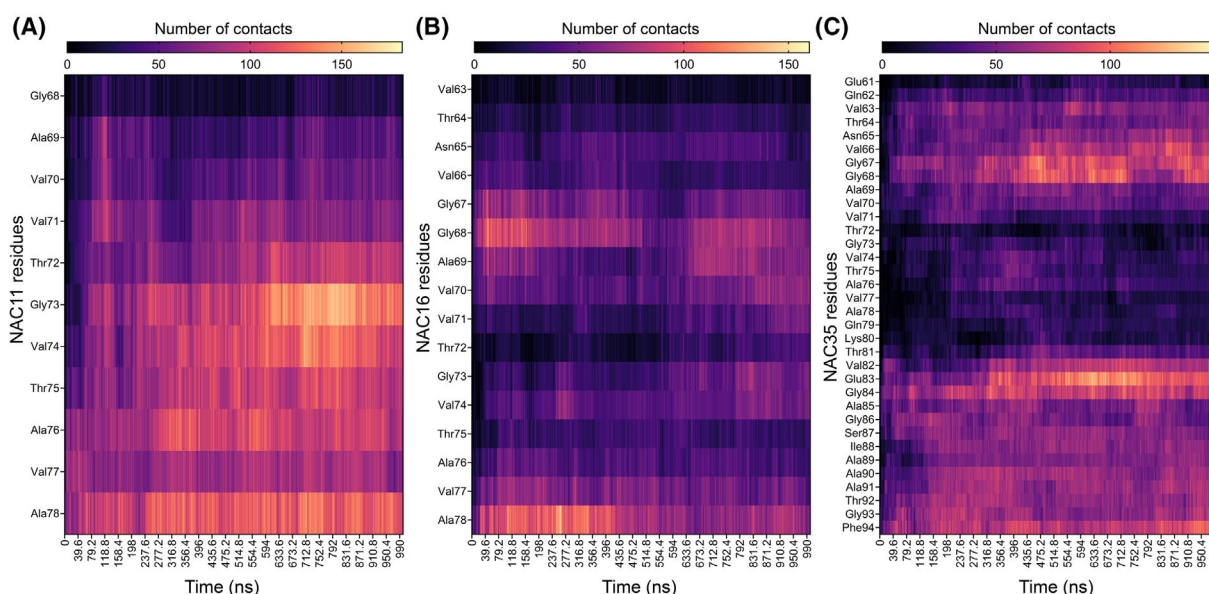


Fig. 10. Residue-level contact analysis between NAC peptides and PB. Heatmaps showing the number of contacts between individual NAC residues and PB (peptide B) in three systems: (A) NAC11 + PB, (B) NAC16 + PB, and (C) NAC35 + PB. Single-trajectory simulation; representative results shown. See Data Availability for access to source data.

NAC11 exhibit faster nucleation than NAC35, this difference is not solely due to the presence of 68–71 (GAVV), as NAC35 also contains this hydrophobic stretch. Previous MD studies have reported that NACore (NAC11) forms stable antiparallel β -sheet dimers with a favorable binding free energy [27–29], identifying it as a critical amyloidogenic sequence. Our experimental results, showing that NAC11 aggregates efficiently and forms dense fibrillar bundles, extend these computational findings, suggesting that secondary interactions beyond dimerization contribute to its aggregation. Instead, NAC35 includes additional N- and C-terminal flanking residues (61–67 and 79–95, respectively) relative to the NAC11 core, which may stabilize transient interactions and reduce hydrophobic exposure, modulating nucleation dynamics.

Notably, the ThT fluorescence of NAC11 and NAC16 rose quickly before declining, a pattern consistent with aggregate precipitation. This atypical behavior may reflect the formation of large aggregates that precipitate and sequester monomers, reducing their concentration, as noted by others for A β aggregation [30]. However, the fibrils formed by NAC16 and NAC11 are less stable and lack the structural integrity required for seeding. While 68–71 contributes to nucleation efficiency, the absence of stabilizing residues (79–95), which are present in NAC35 but lacking in NAC16 and NAC11, may prevent them from maintaining the fibril architecture necessary for effective

templating and seeding [31,32]. Conversely, NAC35, which includes these stabilizing residues, shows slower nucleation but forms fibrils with enhanced stability and robust seeding competency.

The increase in the α Syn dimer-to-monomer ratio observed in the presence of preformed NAC35 fibrils indicates that these fibrils enhance aggregation-prone interactions, aligning with their observed seeding activity. The detection of SDS-resistant dimers may reflect the formation of stable β -sheet-mediated intermediates, as supported by MD simulations showing that NACore peptides form thermodynamically favored antiparallel β -sheet dimers that resist dissociation even under aqueous conditions [29]. In contrast, NAC16 and NAC11 fibrils did not promote dimerization or aggregation, further confirming their lack of seeding competency. This dual analysis of lag time and endpoint fibril formation reveals the interplay between residues critical for nucleation and those promoting stability [31,32]. It further explains how specific segments within the NAC region may collectively drive α Syn aggregation and its pathological behavior. Table 1 summarizes the key findings on truncated NAC peptides and their contributions to nucleation dynamics, fibril stability, seeding competency, and responses to inhibitors.

While multiple hydrophobic segments exist within the NAC domain, including hydrophobic or particularly hydrophobic stretches such as residues 88–91 and

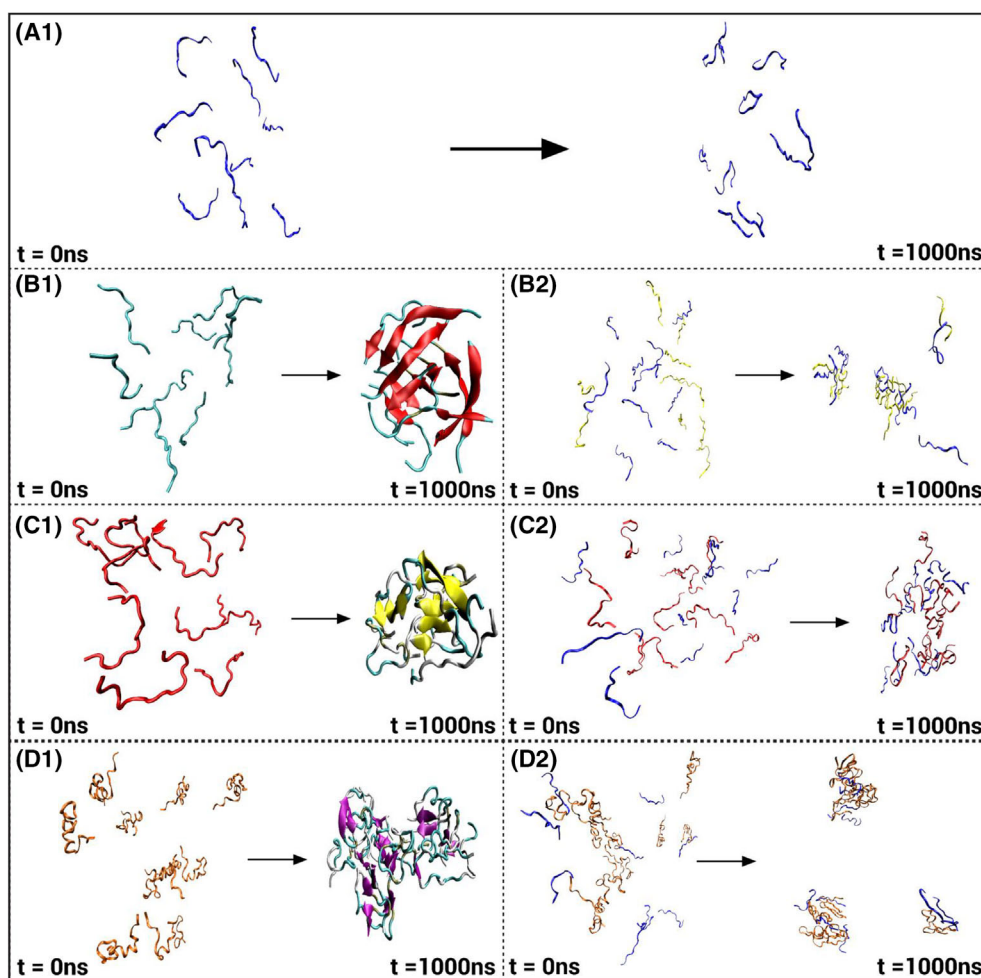


Fig. 11. Structural evolution of NAC peptides in the presence and absence of PB inhibitor. Representative molecular frames at $T = 0$ and $T = 1000$ ns are shown for: (A) PB (peptide B; purple), (B1) NAC11 (cyan) and (B2) NAC11 with PB (purple), (C1) NAC16 (red) and (C2) NAC16 with PB (purple), (D1) NAC35 (orange) and (D2) NAC35 with PB (purple). Prepared using vmd (Visual Molecular Dynamics) software.

76–78, our study focused on residues 68–71 due to their demonstrated role in nucleation efficiency and fibril formation. The elimination of aggregation upon truncation of this region suggests it serves as a critical determinant of aggregation dynamics. Furthermore, its central positioning within the NAC domain aligns with previously identified aggregation-prone motifs, reinforcing its relevance as a therapeutic target. Peptide inhibitors targeting the hydrophobic NAC region further elucidated the role of specific NAC residues in seeding competency. All inhibitors effectively blocked recombinant α Syn aggregation and reduced insoluble fibril formation. The observed reduction in SDS-resistant α Syn dimers in the presence of inhibitors may reflect an alteration in early aggregation behavior, although the specific structural intermediates remain unclear. Given that the prion-like behavior of α Syn

fibrils relies on their structural features [33–35], the loss of seeding competency in fibrils formed in the presence of inhibitors underscores the importance of these structural disruptions.

The distinct responses of NAC16 and NAC11, which have fewer hydrophobic residues than NAC35, are consistent with the idea that inhibitors act on nucleation-relevant segments within the NAC domain, such as the 68–71 (GAVV) motif or nearby hydrophobic residues [17]. The significant delay in aggregating these truncated NAC peptides in the presence of inhibitors indicates the disruption of the hydrophobic interaction needed for nucleation. In contrast, NAC35 showed a shortened lag time in the presence of inhibitors.

The acceleration of aggregation likely arises from the transient stabilization of early aggregation

Table 1. Summary of aggregation properties and inhibitor effects of NAC peptides. Key findings on nucleation dynamics, fibril stability, seeding competency, and responses to inhibitors for truncated NAC peptides. The results emphasize the roles of core and flanking residues in aggregation and provide comparisons with previous studies.

Peptide	NAC residues	α Syn residues	Key observations	Inhibitor effect	Comparison with prior findings
NAC35	1–35	61–95	Slow nucleation; forms robust fibrils with enhanced stability and effective seeding of α Syn aggregation	Disrupts nucleation and reduces fibril formation	Extends Bodles <i>et al.</i> [18]; Highlights the role of 79–95 in enhancing fibril stability and seeding beyond core regions (68–76)
NAC17	19–35	79–95	No nucleation or fibril formation observed.	Not applicable (no aggregation observed)	Shows that 79–95 alone does not aggregate but contributes to stability when paired with NACore residues (68–78)
NAC16	3–18	63–78	Rapid nucleation; moderately stable fibrils; lacks seeding ability	Delays nucleation and reduces fibril formation	Builds on Bodles <i>et al.</i> [18]; Demonstrates that flanking residues (63–67, 72–78) enhance aggregation but are insufficient for fibril stability or seeding
NAC12	11–22	71–82	No nucleation or fibril formation observed	Not applicable (no aggregation observed)	Contradicts Giasson <i>et al.</i> [19]; Shows 71–82 alone cannot form fibrils, indicating flanking residues are required for aggregation
NAC11	8–18	68–78	Rapid nucleation; forms unstable fibrils prone to precipitation; lacks seeding ability	Disrupts nucleation and reduces fibril formation	Builds on Rodríguez <i>et al.</i> [16]; Confirms NACore (68–78) as essential for nucleation but insufficient for fibril stability or seeding
NAC8	12–19	72–79	No nucleation or fibril formation observed	Not applicable (no aggregation observed)	Extends Bodles <i>et al.</i> [18]; Confirms residues 72–79 alone cannot aggregate, emphasizing the indispensability of 68–71 for aggregation

intermediates involving hydrophobic residues such as 68–71. While inhibitors appear to disrupt hydrophobic contacts across all NAC variants, the longer NAC35 sequence may enable partial self-association prior to full inhibitor engagement. This biphasic behavior may reflect an initial phase of partial aggregation facilitated by NAC35's extended sequence, followed by inhibitor-mediated disruption of fibril integrity.

This interpretation is supported by SEM images, which show that fibrils formed by NAC35 in the presence of inhibitors, particularly PB, are shorter and more fragmented than in the control condition, consistent with the reduced endpoint ThT signals. These morphological effects were not limited to NAC35; NAC16 and NAC11 also showed disrupted fibril architecture under inhibitor treatment. Although their endpoint ThT signals did not decrease substantially, the delayed aggregation kinetics and fragmented SEM morphology suggest that inhibitors impair early fibril assembly and structural maturation.

MD simulations further reinforced this mechanism by revealing how PB interacts with aggregation-prone NAC sequences at the atomic level. Using 1- μ s trajectories and unbiased, coil-like starting structures, the simulations showed that PB alters hydrogen bonding patterns and interacts with key hydrophobic segments

of NAC within the simulation timescale. Residue-level contact analysis confirmed that PB interacts most robustly with NAC11, spanning A69 to A78, followed by NAC16 and NAC35, consistent with their differential sensitivity to PB in aggregation assays.

These observations are consistent with the greater sensitivity of NAC11 and NAC16 to PB observed in the aggregation assays. In contrast, the extended sequence in NAC35 shows a more distributed interaction pattern, which may contribute to differences in inhibitor response observed experimentally. These structural observations reinforce the functional relevance of the broader A69–A78 region, which overlaps with the 68–71 (GAVV) motif, as a targetable nucleation determinant, and are consistent with the dual effects observed experimentally of PB on nucleation and elongation.

While truncated peptides are powerful tools for dissecting sequence-specific contributions to aggregation, they simplify the broader aggregation process and do not capture the complexity of full-length α Syn, where long-range inter-domain interactions further modulate aggregation dynamics. Nonetheless, our simulations show that PB alters peptide–peptide interaction patterns and that NAC peptides remain more spatially separated during the simulation period. These findings

complement the experimental data by highlighting how PB interacts with specific NAC regions *in silico*. While our extended single-trajectory simulations yielded consistent and interpretable trends across NAC variants, we acknowledge that the inclusion of replicate runs would strengthen statistical confidence and should be considered in future work. Building on these insights, further work incorporating full-length α Syn, site-specific mutagenesis across NAC, and simulations of higher-order assemblies will be essential to evaluate how early inhibitory interactions affect later stages of fibril propagation.

Collectively, this work advances the understanding of α Syn aggregation by integrating biochemical, structural, and computational approaches and highlights 68–71 (GAVV) and its flanking residues as functionally central and therapeutically targetable elements in synucleinopathies.

Materials and methods

NAC peptides and recombinant α Syn

NAC35, NAC17, NAC16, NAC12, NAC11, and NAC8 peptides were custom-designed and synthesized by GenScript Biotech (Piscataway, NJ, United States) with a purity of $\geq 95\%$. The lyophilized peptides were dissolved in sterile DMSO according to the manufacturer's instructions and stored at -80°C until further use.

Inhibitor peptides (PD, PL, and PB) and the scrambled control peptide were custom-synthesized by Mimotopes (Mulgrave, Victoria, Australia) using standard Fmoc solid-phase peptide synthesis on automated synthesizers. Peptides were purified by preparative HPLC and verified by electrospray mass spectrometry. Each peptide was supplied with a certificate of analysis, including HPLC and MS profiles with a purity of $> 95\%$. The inhibitor peptides were dissolved in sterile MilliQ water and stored at -20°C until use. The expression and purification of recombinant human α Syn (A53T) protein were done as described previously [20].

Hydrophobicity analysis

Hydropathy analysis of NAC peptides was performed using the Kyte-Doolittle hydropathy scale [21] via the ProtScale tool (ExPASy). Different window sizes were selected based on peptide length to balance the smoothing of hydropathy profiles with resolution: window size 7 for longer peptides (NAC35, NAC17, NAC16), window size 5 for intermediate peptides (NAC12, NAC11), and window size 3 for the shortest peptide (NAC8). Positive hydropathy values indicate hydrophobic residues, while negative values reflect hydrophilic residues.

Aggregation kinetics

NAC peptides stored at -80°C were thawed on ice and centrifuged at 12 100 *g* for 45 s. A reaction mixture (40 μL) was prepared on ice containing 100 μM NAC peptide, either alone or in combination with inhibitor peptides at a 1 : 2 molar ratio, along with 15 μM ThT (Sigma-Aldrich, Burlington, MA, USA; Cat. # T3516-5G) in 1 \times PBS (pH 7.2). This mixture was then dispensed into a clear-bottom, black 384-well plate (Revvity, Waltham, MA, USA), and the plate was sealed with a TopSealA-PLUS (Revvity) to prevent evaporation.

The aggregation kinetics was monitored on an EnSpire Multimode Plate Reader (Revvity) at 37°C with a constant agitation of 1000 rpm. To prevent condensation in the assay plate, the upper heater temperature in the plate reader was set to 2°C higher than the lower heater temperature. ThT (Ex: 460–490 nm, Em: 500–550 nm) fluorescence readings were recorded every 5–10 min for 48–72 h. The aggregation lag time was determined by fitting a Boltzmann sigmoidal equation to the fluorescence data in OriginPro 2024 (OriginLab Corporation, Northampton, MA, USA).

For monitoring the effect of inhibitor peptides on α Syn aggregation, recombinant α Syn was incubated with PD, PL, PB, or scrambled peptides at a 1 : 2 molar ratio (100–150 μM α Syn:200–300 μM inhibitor) in the presence of 50 μM ThT. The incubation was performed at 37°C with constant agitation at 850 rpm in a Turbo Thermo Shaker (TMS-200; Allsheng, Hangzhou, China). The formation of amyloid fibrils was monitored by measuring ThT fluorescence over 72 h, as described previously [20].

Fractionation and quantification of fibril concentration

To fractionate aggregated samples (recombinant α Syn or NAC peptides), 20% of the aggregation mixture was set aside as the 'total fraction'. The remaining sample was centrifuged at room temperature at 65 000 *g* for 1 h. The supernatant was collected as the 'soluble fraction' and transferred to a fresh tube. The pellet was resuspended in 80 μL of 1 \times PBS (pH 7.2) and centrifuged at 65 000 *g* for 1 h. After removing the supernatant, the pellet was resuspended in 8 μL of 1 \times PBS (pH 7.2), yielding a 10 \times concentrated 'insoluble fraction'.

The concentration of the total fraction was measured using the Pierce™ BCA Protein Assay Kit (Thermo Fisher Scientific Inc., Waltham, MA, USA, Cat. # 23225). To estimate α Syn fibril concentration in the insoluble fraction, the decrease in monomer concentration in the soluble fraction was quantified by measuring the concentration before and after aggregation. The difference was used to estimate the concentration of fibrils formed.

ANS assay

A 40- μ L reaction mixture was prepared on ice containing 100 μ M NAC peptides and 40 μ M 8-anilino-1-naphthalenesulfonic acid (ANS; Sigma-Aldrich, Cat. # A1028-5G) in 1 \times PBS at pH 4.2, 7.2, or 8.0. The aggregation kinetics were monitored on an EnSpire Multimode Plate Reader (Revvity) at 37 °C with a constant agitation of 1000 rpm. ANS fluorescence readings (Ex: 390 nm, Em: 475 nm) were recorded every 5–10 min for 48–72 h. The lag time of aggregation was determined by fitting a Boltzmann sigmoidal equation, as described in the previous section.

UV–vis spectrophotometric analysis

NAC peptides (100 μ M) were incubated without ThT for 48 h to allow aggregation. The resulting mixtures were centrifuged at 65 000 *g* for 1 h to separate the soluble and insoluble fractions, as outlined above. Insoluble fractions were resuspended in an equal volume of 1 \times PBS (pH 7.2) as the soluble fractions. UV–Vis absorption spectra were recorded from 400 to 600 nm using an EnSpire Multimode Plate Reader (Revvity) with a resolution of 10 nm.

Atomic force microscopy

NAC peptide aggregates, collected after 48 h of the aggregation assay, were dropped onto a freshly cleaved 10 mm AFM mica disc (Ted Pella, Inc., Redding, CA, USA) and air-dried for 10 min at room temperature. The mica discs were washed five times with deionized water and then dried for 10–15 min at room temperature. AFM imaging was performed as described [36], using the SCANASYST AIR probe (tip radius: 2 nm, spring constant: 0.4 N/m).

Transmission electron microscopy

Samples were dropped on glow-discharged carbon-coated copper grids and negatively stained with 2% uranyl acetate. Electron microscopy was performed on a Tecnai G2 F20 microscope (FEI Technologies, Hillsboro, OR, USA) with an Eagle 4K CCD camera (FEI Technologies) or a CM100 TWIN Transmission Electron Microscope (Philips, Amsterdam, Netherlands) equipped with a side-mounted Veleta Camera (Olympus, Tokyo, Japan) and processed in the iTEM software suite (Olympus). After bringing the images to 2048 \times 2048 pixels, the pixel size at the specimen level was 1.14 nm. Approximately 20 micrographs of each specimen were recorded and evaluated.

In vitro seeding assay

For the *in vitro* seeding assay, α Syn (100 μ M), NAC35 (100 μ M), NAC16 (200 μ M), and NAC11 (200 μ M) peptides

were aggregated without ThT for 72–96 h. Fibril formation was confirmed by mixing 10 μ L of the aggregated sample with 15 μ M ThT and measuring fluorescence using an EnSpire Multimode Plate Reader (Revvity). Aggregates were then centrifuged to separate insoluble fractions as described above.

α Syn (100 μ M) was incubated with 25 μ M insoluble fractions (preformed fibrils) of α Syn, NAC35, NAC16, and NAC11 in a 100–150 μ L volume per well of a 96-well ViewPlate in the presence of 50 μ M ThT. The aggregation kinetics were monitored on an EnSpire Multimode Plate Reader (Revvity) at 37 °C with a constant agitation of 1000 rpm. ThT fluorescence was recorded every 5–10 min for over 60–65 h. After aggregation, the contents of each well were collected, and insoluble fractions were isolated by centrifugation. These fractions were subsequently analyzed using dot blot analysis and Coomassie gel staining.

Coomassie gel staining

The samples were mixed with 2 \times Laemmli buffer [62.5 mM Tris/HCl (pH 6.8), 25% (w/v) glycerol, 2% SDS, and 0.01% Bromophenol Blue, supplemented with 5% (v/v) 2-mercaptoethanol] and boiled at 95 °C for 5 min. The samples were then subjected to electrophoresis using Mini-PROTEAN TGX 4–20% Precast gels (Bio-Rad, Hercules, CA, USA, Cat. # 4561095) in Tris/glycine/SDS running buffer (Bio-Rad). Gels were fixed in 50% methanol (v/v) and 10% acetic acid (v/v) for 1 h, stained with Coomassie Brilliant Blue R-250 Staining Solution (Bio-Rad, Cat. # 1610436EDU) for 12 h at 4 °C with gentle agitation, and destained in deionized water. Gel images were acquired using a ChemiDoc MP imaging system (Bio-Rad), and densitometry was performed using the IMAGEJ software (RRID: SCR_003070; Bethesda, MD, USA).

Dot blot analysis

Five μ L of the sample (2.5 μ L first, allowed to dry completely, then another 2.5 μ L) was spotted onto a nitrocellulose membrane (Bio-Rad, Cat. # 1620147), pre-divided into uniform circular grids, and allowed to dry for 10 min at room temperature. The membrane was blocked for 1 h with 5% bovine serum albumin (BSA) in 1 \times Tris-buffered saline with 0.05% Tween® 20 (TBST), followed by 3 \times washes with TBST. The membrane was then incubated for 1 h with anti- α -Synuclein (D37A6) rabbit monoclonal antibody (Cell Signaling Technology, Inc., Danvers, MA, USA, Cat. # 4179, RRID: AB_1904156), which recognizes an epitope surrounding Glu105 in the C-terminal region of α Syn, and was used at a 1 : 2000 dilution in 5% BSA/TBST. After 3 \times washes with TBST, the blot was incubated with Alexa Fluor™ 647 Goat anti-Rabbit IgG (Thermo Fisher Scientific; Cat. # A-21245) at a 1 : 5000

dilution for 1 h. The blot was imaged using the ChemiDoc MP imaging system (Bio-Rad), and densitometry was performed using IMAGEJ.

Microscale thermophoresis

The binding affinity of the inhibitor peptide was measured by microscale thermophoresis (MST) using a Nanotemper Monolith NT.115 instrument (Nanotemper Technologies GmbH, Munich, Germany). Recombinant α Syn was freshly labeled with the Monolith His-Tag RED tris-NTA labeling dye according to the manufacturer's protocol (Nanotemper Technologies GmbH). Measurements were conducted in MST buffer (50 mM Tris, 250 mM NaCl, pH 7.0) using standard capillaries (K002; Nanotemper Technologies GmbH). The final concentration of the labeled α Syn in the assay was 50 nM. Binding reactions were incubated on ice for 5 min; then centrifuged at 20 000 *g* before loading into the standard glass capillaries (Monolith NTCapillaries, Nano Temper Technologies GmbH). All the measurements were performed with the LED set to 20% intensity and the MST power set to 50%. The laser on-time was 30 s, and the off-time was 5 s.

Scanning electron microscopy of NAC samples

NAC peptides aggregated in the absence or presence of inhibitor peptides, as described in the section Aggregation Kinetics, were collected and pooled into Eppendorf tubes. Approximately 2 μ L of each sample was drop-cast onto a silicon wafer and air-dried at room temperature. No fixation or sputter coating was applied before imaging.

SEM imaging was performed using a Zeiss Sigma 360 VP microscope (Carl Zeiss Microscopy GmbH, Oberkochen, Germany) at an accelerating voltage of 1 kV with a working distance of approximately 2 mm, under high vacuum conditions. Images were acquired using an InLens secondary electron detector at magnifications of approximately 115 \times and 958 \times , selected based on fibril morphology. Aperture settings remained consistent across all samples. Post-acquisition, brightness and contrast were adjusted uniformly across images to enhance visibility while preserving structural integrity.

Cell seeding assay

HEK293T α Syn (A53T) CFP/YFP biosensor cells (HEK293T parental line, [RRID:CVCL_0063](#)) were kindly provided by Dr. Marc Diamond from the University of Texas Southwestern Medical Center (Dallas, TX, USA). The cells were not further authenticated but were routinely tested and confirmed to be mycoplasma-free using PCR-

based assays. The cells were maintained in complete growth media consisting of 88% Dulbecco's modified Eagle's growth medium (Lonza, Walkersville, MD, USA, Cat. # 12-604F), supplemented with 10% (v/v) fetal bovine serum (Thermo Fisher Scientific Inc., Cat. # A5256701), 10 mM HEPES (Serana Europe GmbH, Brandenburg, Germany; Cat. # BSL-001-100ML), 1% (v/v) GlutaMAXTM Supplement (Thermo Fisher Scientific Inc., Cat. # 35050061), and 1% (v/v) Penicillin–Streptomycin Solution (Thermo Fisher Scientific Inc., Cat. # 15140130). Cells were maintained at 37 °C in a humidified incubator with 5% CO₂/atmospheric air.

Cells were plated in 96-well Phenoplate (Revvity, Cat. #6057802; 5000 cells per 100 μ L) or 24-well plate (20 000 cells per 1 mL) in complete growth media. Both plates were pre-coated overnight with 50 μ g·mL⁻¹ Poly-D-Lysine (Sigma-Aldrich, Cat. # P6407). The following day, cells were transfected with the total fraction (containing both monomers and fibrils) or the insoluble fraction (containing primarily fibrils) of the α Syn aggregation reaction. These fractions were prepared by aggregating α Syn with or without inhibitors. Transfection mixtures were prepared by combining 1 μ M of the total fraction or insoluble fraction, or an equivalent concentration of only inhibitor peptides, in 20 μ L (for 96-well plate) or 100 μ L (for 24-well plate) of Opti-MEMTM I Reduced Serum Medium (Thermo Fisher Scientific Inc., Cat. #11058021), supplemented with 0.5 μ L (96-well plate) or 4 μ L (24-well plate) TurboFectTM Transfection Reagent (Thermo Fisher Scientific Inc., Cat. # R0531). Controls included mixtures with Opti-MEM and TurboFectTM but without α Syn or Opti-MEM and α Syn but without TurboFectTM. Before preparation of the transfection mixtures, α Syn samples were sonicated using Branson UltrasonicTM Sonifier Cup Horns (Marshall Scientific, Hampton, NH, USA) with settings: 50% amplitude, 30 s ON, 10 s OFF, for a total of 1 min, to break fibrils into smaller fragments. The transfection mixture was briefly vortexed and incubated at room temperature for 15 min before adding to the cells. Twenty milliliters (for 96-well plate) or 100 μ L (for 24-well plate) of transfection mixture was added dropwise to the cells, and the plate was gently tapped to mix the contents. After 72 h, cells were either fixed directly in the plates for imaging or harvested using 0.5% Trypsin–EDTA (Thermo Fisher Scientific Inc., Cat. # 15400054) and then fixed for flow cytometric analysis. Fixed cells in 96-well plates were washed once with 1 \times PBS and stained with 10 μ M Hoechst-33 342 nuclear dye (Invitrogen, Carlsbad, CA, USA, Cat. #H21492) diluted in PBS for 10 min at room temperature. To preserve the cells for imaging, a 1% glycerol solution prepared in deionized water was added to each well. For flow cytometric analysis, trypsinized cells from 3 wells per experiment condition were pooled, fixed with 2% paraformaldehyde, washed once with PBS, and then resuspended in PBS for further processing.

Quantification of CFP/YFP inclusions

Cells were imaged using a high-content imaging system (Cell Voyager 7000S; Yokogawa, Tokyo, Japan) with a 20 \times objective. CFP/YFP inclusions of α Syn (A53T) were detected using a 488 nm laser line (Ex = 460–490 nm, Em = 500–550 nm), while Hoechst-33 342-stained nuclei were detected using the 405 nm laser line (Ex = 360–400 nm, Em = 410–480 nm). At least 10 focal areas per well were imaged for each experimental replicate. Acquired images were processed using Signals Image Artist (Revvity). The number of cells quantified by Hoechst-stained nuclei and the number of CFP/YFP inclusions used to quantify intracellular seeding were analyzed using an image analysis script in Signals Image Artist (see Appendix S1). The total number of inclusions per well was normalized to cell confluency.

Flow cytometry analysis cell seeding

Cells were analyzed on a FACSaria II Sorpe flow cytometer (BD Biosciences, Franklin Lakes, NJ, USA). Initially, 50 000 cells were acquired to set up gating. Dead cells and debris were excluded using forward scatter versus side scatter gating. Intact cells were then gated and analyzed in the blue/green channels. The gating strategy to identify cells with aggregates (P2 gate) was based on the expression levels of fluorescent protein tags (CFP/YFP). YFP was excited with a 488 nm laser, and emission was detected by a 525/50 nm (green) bandpass filter. CFP was excited with a 445 nm laser, and emission was detected by a 530/30 nm (blue) bandpass filter. The integrated FRET density was calculated by multiplying the percentage of FRET-positive cells by their median fluorescence intensity within the FRET-positive gate, as previously described [24]. This density was then normalized for treated groups relative to untreated controls (cells not exposed to fibrils). Data analysis was performed using BD FACSDiva™ Software.

MD simulation

MD simulations were conducted using the GROMACS package with parameters from the GROMOS-53A6 force field [37,38]. Initial peptide structures were obtained from the AlphaFold3 web server [39] and subjected to a 100 ns equilibration simulation to allow relaxation into coil-rich conformations, appropriate for disordered NAC peptides in aqueous solution. Final conformations from this pre-simulation step were used to initiate the main 1000 ns production runs. Each system consisted of equimolar amounts of PB and a given NAC peptide (NAC35, NAC16, or NAC11), with 10 PB and 10 NAC peptides randomly placed in a cubic simulation box ($\sim 10 \times 10 \times 10 \text{ nm}^3$), ensuring a minimum 1.0 nm distance between peptides and

box edges to avoid interactions from periodic images. Systems were solvated using the SPC/E water model [40], electrically neutralized, and energy minimized using the steepest descent algorithm until the maximum force on atoms was $< 10 \text{ kJ}\cdot\text{mol}^{-1}\cdot\text{nm}^{-1}$. Temperature was maintained at 300 K using the V-rescaling thermostat [41] and pressure at 1 bar using the Parrinello-Rahman barostat [42]. Short-range non-bonded interactions were calculated with a 1.2 nm cutoff, and long-range electrostatics were handled using the Particle Mesh Ewald method. A 2-fs time-step was used for all simulations. Simulation trajectories were analyzed using GROMACS utilities and vmd software [43]. A detailed summary of each system's composition and simulation setup is provided in Table S1.

Statistics analysis

Data are presented as mean \pm SEM ($n \geq 2$ independent experiments, unless stated otherwise). One-way ANOVA tests were utilized to compare means across multiple groups within a single factor. Multiple comparisons for ANOVA tests were performed using Tukey's. Statistical significance was set at $P < 0.05$. *F* values and degrees of freedom for all ANOVA analyses are summarized in Tables S2–S6.

Acknowledgements

This work was supported by funding from the National Institute for Neurological Research (Program EXCELES, ID Project No. LX22NPO5107) funded by the European Union - Next Generation EU from the Ministry of Education, Youth and Sports of the Czech Republic (MEYS), and the project TN02000109 (Personalized Medicine: From Translational Research into Biomedical Applications, co-financed with the state support of the Technology Agency of the Czech Republic as part of the National Centers of Competence Program), and the Grant Agency of the Czech Republic (23-06301J). Additional support in parts was received from infrastructural projects (CZ-OPEN-SCREEN—LM2023052; EATRIS-CZ—LM2023053), the Czech biobank network (BBMRI – LM2023033), large RI Projects (Czech-BioImaging—LM2023050; LM2018129), and the National Institute for Cancer Research (Program EXCELES, ID Project No. LX22NPO5102). SM, SM, SH, and MN acknowledge the research council of Tarbiat Modares University. MN and SH were visiting scientists at Palacky University, supported by the European Commission through a grant (VIDEC: 872195). The authors thank Dr Marc Diamond at the University of Texas Southwestern Medical Center for providing alpha-synuclein biosensor cells. Open access publishing facilitated by

Univerzita Palackeho v Olomouci, as part of the Wiley - CzechELib agreement.

Conflict of interest

The authors declare no conflict of interest.

Author contributions

VD: conceptualization, methodology, investigation, interpretation, funding acquisition, supervision, and writing – original draft, review, and editing. SMMM: methodology, investigation. NA: methodology, investigation. SS: methodology and investigation. FM: methodology and investigation. SM: methodology and investigation. LM: methodology and investigation. MK: methodology and investigation. VR: investigation, interpretation, visualization. IF: methodology and investigation. RK: methodology and investigation. SH: methodology, investigation, and interpretation. MH: resources and funding acquisition. MN: methodology, investigation, interpretation, funding acquisition, and writing – original draft, review, and editing.

Peer review

The peer review history for this article is available at <https://www.webofscience.com/api/gateway/wos/peer-review/10.1111/febs.70222>.

Data availability statement

Source data supporting this study are available in Zenodo at DOI: [10.5281/zenodo.15271406](https://doi.org/10.5281/zenodo.15271406), including raw experimental and simulation data for Figs 1–6, 8–10, and Figs S2–S4. Additional data supporting the findings are provided within the article and its [Supplementary Materials](#).

References

- de Oliveira GAP & Silva JL (2019) Alpha-synuclein stepwise aggregation reveals features of an early onset mutation in Parkinson's disease. *Commun Biol* **2**, 374.
- Kumar ST, Mahul-Mellier A-L, Hegde RN, Rivière G, Moons R, Ibáñez de Opakua A, Magalhães P, Rostami I, Donzelli S, Sobott F *et al.* (2022) A NAC domain mutation (E83Q) unlocks the pathogenicity of human alpha-synuclein and recapitulates its pathological diversity. *Sci Adv* **8**, eabn0044.
- Privat C, Madurga S, Mas F & Rubio-Martinez J (2022) Molecular dynamics simulations of an α -synuclein NAC domain fragment with a ff14IDPSFF IDP-specific force field suggest β -sheet intermediate states of fibrillation. *Phys Chem Chem Phys* **24**, 18841–18853.
- Delenclos M, Burgess JD, Lamprokostopoulou A, Outeiro TF, Vekrellis K & McLean PJ (2019) Cellular models of alpha-synuclein toxicity and aggregation. *J Neurochem* **150**, 566–576.
- Boza-Serrano A, Reyes JF, Rey NL, Leffler H, Bousset L, Nilsson U, Brundin P, Venero JL, Burguillos MA & Deierborg T (2014) The role of galectin-3 in α -synuclein-induced microglial activation. *Acta Neuropathol Commun* **2**, 156.
- Vargas JY, Grudina C & Zurzolo C (2019) The prion-like spreading of α -synuclein: from in vitro to in vivo models of Parkinson's disease. *Ageing Res Rev* **50**, 89–101.
- Peelaerts W, Bousset L, Van der Perren A, Moskalyuk A, Pulizzi R, Giugliano M, Van den Haute C, Melki R & Baekelandt V (2015) α -Synuclein strains cause distinct synucleinopathies after local and systemic administration. *Nature* **522**, 340–344.
- Zhang P & Liu B (2019) Association between Parkinson's disease and risk of cancer: a PRISMA-compliant meta-analysis. *ACS Chem Neurosci* **10**, 4430–4439.
- Yang H-M, Cheng Y-Z, Hou T-Z, Fan J-K, Gu L, Zhang J-N & Zhang H (2023) Upregulation of Parkinson's disease-associated protein alpha-synuclein suppresses tumorigenesis via interaction with mGluR5 and gamma-synuclein in liver cancer. *Arch Biochem Biophys* **744**, 109698.
- Filippou PS & Outeiro TF (2021) Cancer and Parkinson's disease: common targets, emerging hopes. *Mov Disord* **36**, 340–346.
- Flagmeier P, Meisl G, Vendruscolo M, Knowles TPJ, Dobson CM, Buell AK & Galvagnion C (2016) Mutations associated with familial Parkinson's disease alter the initiation and amplification steps of α -synuclein aggregation. *Proc Natl Acad Sci USA* **113**, 10328–10333.
- Ulamet SM, Maya-Martinez R, Byrd EJ, Dewison KM, Xu Y, Willis LF, Sobott F, Heath GR, van Oosten Hawle P, Buchman VL *et al.* (2022) Single residue modulators of amyloid formation in the N-terminal P1-region of α -synuclein. *Nat Commun* **13**, 4986.
- Paslawski W, Mysling S, Thomsen K, Jørgensen TJD & Otzen DE (2014) Co-existence of two different α -synuclein oligomers with different core structures determined by hydrogen/deuterium exchange mass spectrometry. *Angew Chem Int Ed* **53**, 7560–7563.
- Li B, Ge P, Murray KA, Sheth P, Zhang M, Nair G, Sawaya MR, Shin WS, Boyer DR, Ye S *et al.* (2018) Cryo-EM of full-length α -synuclein reveals fibril polymorphs with a common structural kernel. *Nat Commun* **9**, 3609.

- 15 Tuttle MD, Comellas G, Nieuwkoop AJ, Covell DJ, Berthold DA, Kloepper KD, Courtney JM, Kim JK, Barclay AM, Kendall A *et al.* (2016) Solid-state NMR structure of a pathogenic fibril of full-length human α -synuclein. *Nat Struct Mol Biol* **23**, 409–415.
- 16 Rodriguez JA, Ivanova MI, Sawaya MR, Cascio D, Reyes FE, Shi D, Sangwan S, Guenther EL, Johnson LM, Zhang M *et al.* (2015) Structure of the toxic core of α -synuclein from invisible crystals. *Nature* **525**, 486–490.
- 17 Waxman EA, Emmer KL & Giasson BI (2010) Residue Glu83 plays a major role in negatively regulating α -synuclein amyloid formation. *Biochem Biophys Res Commun* **391**, 1415–1420.
- 18 Bodles AM, Guthrie DJS, Greer B & Irvine GB (2001) Identification of the region of non-a β component (NAC) of Alzheimer's disease amyloid responsible for its aggregation and toxicity. *J Neurochem* **78**, 384–395.
- 19 Giasson BI, Murray IVJ, Trojanowski JQ & Lee VM-Y (2001) A hydrophobic stretch of 12 amino acid residues in the middle of α -synuclein is essential for filament assembly. *J Biol Chem* **276**, 2380–2386.
- 20 Rezaeian N, Shirvanizadeh N, Mohammadi S, Nikkhah M & Arab SS (2017) The inhibitory effects of biomimetically designed peptides on α -synuclein aggregation. *Arch Biochem Biophys* **634**, 96–106.
- 21 Kyte J & Doolittle RF (1982) A simple method for displaying the hydropathic character of a protein. *J Mol Biol* **157**, 105–132.
- 22 Hoyer W, Antony T, Cherny D, Heim G, Jovin TM & Subramaniam V (2002) Dependence of α -synuclein aggregate morphology on solution conditions. *J Mol Biol* **322**, 383–393.
- 23 Flynn JD, McGlinchey RP, Walker RL & Lee JC (2018) Structural features of α -synuclein amyloid fibrils revealed by Raman spectroscopy. *J Biol Chem* **293**, 767–776.
- 24 Holmes BB, Furman JL, Mahan TE, Yamasaki TR, Mirbaha H, Eades WC, Belaygorod L, Cairns NJ, Holtzman DM & Diamond MI (2014) Proteopathic tau seeding predicts tauopathy in vivo. *Proc Natl Acad Sci USA* **111**, E4376–E4385. doi: [10.1073/pnas.1411649111](https://doi.org/10.1073/pnas.1411649111)
- 25 Peña-Díaz S, Pujols J, Vasili E, Pinheiro F, Santos J, Manglano-Artuñedo Z, Outeiro TF & Ventura S (2022) The small aromatic compound SynuClean-D inhibits the aggregation and seeded polymerization of multiple α -synuclein strains. *J Biol Chem* **298**, 101902.
- 26 Murray KA, Hu CJ, Pan H, Lu J, Abskharon R, Bowler JT, Rosenberg GM, Williams CK, Elezi G, Balbirnie M *et al.* (2023) Small molecules disaggregate alpha-synuclein and prevent seeding from patient brain-derived fibrils. *Proc Natl Acad Sci USA* **120**, e2217835120.
- 27 Huang R, Tang R, Song X, Wang J, Chen K & Tian W (2023) Insights into aggregation dynamics of NACore peptides from coarse-grained simulations. *Proteins* **91**, 16–21.
- 28 Martins GF, Nascimento C & Galamba N (2023) Mechanistic insights into polyphenols' aggregation inhibition of α -synuclein and related peptides. *ACS Chem Neurosci* **14**, 1905–1920.
- 29 Yamauchi M & Okumura H (2021) Dimerization of α -synuclein fragments studied by isothermal–isobaric replica-permutation molecular dynamics simulation. *J Chem Inf Model* **61**, 1307–1321.
- 30 Berntsson E, Vosough F, Svantesson T, Pansieri J, Iashchishyn IA, Ostojić L, Dong X, Paul S, Jarvet J, Roos PM *et al.* (2023) Residue-specific binding of Ni(II) ions influences the structure and aggregation of amyloid beta (a β) peptides. *Sci Rep* **13**, 3341.
- 31 Lam HT, Graber MC, Gentry KA & Bieschke J (2016) Stabilization of α -synuclein fibril clusters prevents fragmentation and reduces seeding activity and toxicity. *Biochemistry* **55**, 675–685.
- 32 Vettore N & Buell AK (2019) Thermodynamics of amyloid fibril formation from chemical depolymerization. *Phys Chem Chem Phys* **21**, 26184–26194.
- 33 Taylor AIP & Staniforth RA (2022) General principles underpinning amyloid structure. *Front Neurosci* **16**, 878869.
- 34 Tarutani A, Suzuki G, Shimozaawa A, Nonaka T, Akiyama H, Hisanaga S & Hasegawa M (2016) The effect of fragmented pathogenic α -Synuclein seeds on prion-like propagation. *J Biol Chem* **291**, 18675–18688.
- 35 Griner SL, Seidler P, Bowler J, Murray KA, Yang TP, Sahay S, Sawaya MR, Cascio D, Rodriguez JA, Philipp S *et al.* (2019) Structure-based inhibitors of amyloid beta core suggest a common interface with tau. *elife* **8**, e46924.
- 36 Annadurai N, Malina L, Malohlava J, Hajdúch M & Das V (2022) Tau R2 and R3 are essential regions for tau aggregation, seeding and propagation. *Biochimie* **200**, 79–86.
- 37 Van Der Spoel D, Lindahl E, Hess B, Groenhof G, Mark AE & Berendsen HJC (2005) GROMACS: fast, flexible, and free. *J Comput Chem* **26**, 1701–1718.
- 38 Oostenbrink C, Soares TA, van der Vegt NFA & van Gunsteren WF (2005) Validation of the 53A6 GROMOS force field. *Eur Biophys J* **34**, 273–284.
- 39 Abramson J, Adler J, Dunger J, Evans R, Green T, Pritzel A, Ronneberger O, Willmore L, Ballard AJ, Bambrick J *et al.* (2024) Accurate structure prediction of biomolecular interactions with AlphaFold 3. *Nature* **630**, 493–500.
- 40 Smith PE & van Gunsteren WF (1994) Consistent dielectric properties of the simple point charge and extended simple point charge water models at 277 and 300 K. *J Chem Phys* **100**, 3169–3174.

- 41 Bussi G, Donadio D & Parrinello M (2007) Canonical sampling through velocity rescaling. *J Chem Phys* **126**, 014101.
- 42 Parrinello M & Rahman A (1981) Polymorphic transitions in single crystals: a new molecular dynamics method. *J Appl Phys* **52**, 7182–7190.
- 43 Humphrey W, Dalke A & Schulten K (1996) VMD: visual molecular dynamics. *J Mol Graph* **14**, 33–38.

Supporting information

Additional supporting information may be found online in the Supporting Information section at the end of the article.

Fig. S1. ThT fluorescence and AFM images of NAC aggregates.

Fig. S2. UV-Vis analysis of NAC peptide total fractions.

Fig. S3. Raman spectroscopy confirms aggregation-induced β -sheet formation in NAC35, NAC16, and NAC11 fibrils.

Fig. S4. ThT kinetics of preformed fibrils.

Fig. S5. Dot blot image and Coomassie-stained gel image for Fig. 3.

Fig. S6. MST traces and dose-response curves for α Syn binding to inhibitor peptides.

Fig. S7. TEM images of α Syn fibrils formed with scrambled peptides.

Fig. S8. ThT kinetics of inhibitor peptides alone.

Fig. S9. Original uncropped image of the dot blot shown in Fig. 4f.

Fig. S10. Coomassie-stained gels for Fig. 4h.

Fig. S11. CFP/YFP inclusion quantifications and FRET flow cytometry side scatter plot.

Fig. S12. High-magnification SEM images of NAC11 fibrils.

Fig. S13. Scanning electron microscope (SEM) images of inhibitor peptides PD, PL, and PB.

Table S1. Details of the components of the MD simulation systems.

Table S2. F values and degrees of freedom for one-way ANOVA performed in Fig. 1c, h–j.

Table S3. F values and degrees of freedom of one-way ANOVA performed in Fig. 3b and d.

Table S4. F values and degrees of freedom of one-way ANOVA performed in Fig. 4b, d, k, and l.

Table S5. F values and degrees of freedom of one-way ANOVA performed in Fig. 5c–e.

Table S6. F values, degrees of freedom, and other details of one-way ANOVA performed in Fig. 6D–G.

Appendix S1. Image Analysis Script to quantify CFP/YFP inclusions and cell confluence.